

# Polarized Neutron Scattering

B. Roessli<sup>1</sup>, P. Böni<sup>2</sup>

<sup>1</sup>Laboratory for Neutron Scattering, ETH Zürich & Paul Scherrer Institute, CH-5232 Villigen PSI

<sup>2</sup> Physik-Department E21, Technische Universität München, D-85748 Garching

November 26, 2024

**Keywords:** polarized neutron beam, polarization analysis, magnetic moment distribution, form factors, spherical neutron polarimetry, paramagnetic scattering, magnetic excitations, diffuse scattering

## Contents

<b>1</b>	<b>Introduction</b>	<b>3</b>
<b>2</b>	<b>Elastic neutron scattering cross-section for polarized neutrons</b>	<b>4</b>
<b>3</b>	<b>Production of polarized neutrons</b>	<b>5</b>
3.1	Single-crystal polarizers . . . . .	5
3.2	Thin films . . . . .	6
3.3	Spin filters . . . . .	6
<b>4</b>	<b>Determination of Form Factors and Spin Densities</b>	<b>8</b>
4.1	Magnetic Form Factors . . . . .	9
4.2	Magnetisation distribution in molecular magnets . . . . .	10
4.3	Spin susceptibility in the high- $T_c$ superconductor $\text{YBa}_2\text{Cu}_3\text{O}_{7-x}$ . . . . .	11
<b>5</b>	<b>Spherical Neutron Polarimetry</b>	<b>12</b>

5.1	Realization of a zero-field chamber: Cryopad . . . . .	13
5.2	Example: UPtGe . . . . .	14
<b>6</b>	<b>Inelastic Neutron Scattering with Polarized Neutrons</b>	<b>15</b>
6.1	Longitudinal neutron polarimetry . . . . .	16
6.2	The XYZ method . . . . .	18
6.3	Paramagnetic scattering . . . . .	18
6.4	Transverse and longitudinal excitations in ferromagnets . . . . .	20
6.5	Spin waves and phasons in incommensurate, antiferromagnetic Cr . . . . .	21
6.6	Magnetic excitations in a heavy fermion superconductor . . . . .	22
6.7	Magnons and Solitons in low-dimensional systems . . . . .	23
<b>7</b>	<b>Self and collective diffusive atomic motions</b>	<b>24</b>
<b>8</b>	<b>Conclusions</b>	<b>25</b>

# 1 Introduction

In the previous chapters of this book, experimental results and the theory of elastic and inelastic neutron scattering have been presented under the assumption that the magnetic moments of the neutrons are randomly oriented. It has been shown that details about the physical properties of a system are extracted by analysing the momentum and the energy of the scattered neutrons. It is intuitively imaginable, however, that measuring the spin state of the neutron after scattering relative to its state before the scattering process should provide us with additional information. To that end the cross-sections for neutron scattering must now also take into account the relationship between the spin of the neutron with the physical properties of the target.

The polarization of a neutron is defined as

$$\mathbb{P} = 2\langle\hat{\mathbf{s}}\rangle = \langle\hat{\boldsymbol{\sigma}}\rangle, \quad (1)$$

where  $\boldsymbol{\sigma}$  are the Pauli matrices. Clearly,  $|\mathbb{P}|$  is equal to 0 for a completely unpolarised beam and  $|\mathbb{P}| = 1$  if the beam is totally polarised. For intermediate values, the neutron beam is not in a well defined state and the spin part of the neutron wave-function must be described by a more general form  $\chi = u\chi_{\uparrow} + v\chi_{\downarrow}$  with  $|u|^2 + |v|^2 = 1$ . That is  $|u|^2$  and  $|v|^2$  are the probabilities that the neutron spin will be *up* or *down*, respectively. If a matrix operator  $\hat{\rho}$  is defined like

$$\hat{\rho} = \chi\chi^{\dagger} = \begin{pmatrix} |u|^2 & uv^{\dagger} \\ vu^{\dagger} & |v|^2 \end{pmatrix} = \frac{1}{2}(\mathbb{I} + \mathbf{P} \cdot \hat{\boldsymbol{\sigma}}), \quad (2)$$

then the polarization of the neutron is described by a three-dimensional *vector* with components  $\mathbf{P} = (2\Re(u^{\dagger}v), 2\Im(u^{\dagger}v), |u|^2 - |v|^2)$  [1]. The polarization of a neutron beam is accordingly defined as  $\mathbf{P} = \frac{1}{N} \sum \mathbf{P}_j$  where  $N$  is the total number of neutrons and the sum runs over the polarization vector of the individual neutrons  $j$ .

The cross-section  $\sigma$  and the polarization of the scattered beam  $\mathbf{P}_f$  can be expressed as a function of the density matrix  $\hat{\rho}$ , the polarization vector of the incident neutrons  $\mathbf{P}_i$  and the interaction potential  $\hat{v}$  between the target and the neutron. In its most general form,  $\mathbf{P}_f = \text{Tr}\hat{\rho}\hat{v}^{\dagger}\hat{\boldsymbol{\sigma}}\hat{v}/\text{Tr}\hat{\rho}\hat{v}^{\dagger}\hat{v}$ .

Neutron scattering with polarized neutrons has been used in fundamental and condensed matter physics since many years despite the low flux of polarized beams. One of the first applications was the study of spin density distributions in ferromagnets, following the pioneering work of Shull and Nathans [2]. In those days the polarization of the scattered neutrons was established by measuring their transmission through a magnetized block of iron. As predicted by Halpern and Johnson [3] the polarization of the scattered neutrons,  $\mathbf{P}_f$ , depends on the orientation of the scattering vector  $\mathbf{Q}$  with respect to the polarization of the incident neutrons,  $\mathbf{P}_i$ , like

$$\mathbf{P}_f = -\hat{Q}(\hat{Q} \cdot \mathbf{P}_i) \quad (3)$$

where  $\hat{Q} = \mathbf{Q}/|\mathbf{Q}|$ . In other words for  $\mathbf{P}_i \parallel \mathbf{Q}$  all magnetic scattering is spin flip. Therefore polarization analysis in neutron scattering provides an excellent method to distinguish between nuclear and magnetic scattering. In 1969 the classic paper by Moon et al. [4] appeared that explains in simple terms one-dimensional polarization analysis (nowadays called longitudinal polarimetry) of neutrons for elastic as well as inelastic neutron scattering. They demonstrated the polarization dependence of the nuclear and magnetic scattering.

Another, rather different application of polarized neutrons is their use for attaining extremely high energy resolution by measuring changes in the neutron beam polarization caused by inelastic scattering. In 1972, Mezei [5] suggested to use the precession of the magnetic moment of the neutrons in a magnetic field as an internal clock. By means of the so-called *neutron spin-echo* technique energy resolutions of the order of nano-electron volts can be achieved enabling the investigation of slow dynamics, for example in the critical region of magnetic systems or in polymers and glasses.

Nowadays, polarized neutron scattering is a fast developing experimental method that finds applications in various fields of condensed-matter research. Examples are

- determination of magnetic structures and spin densities,
- identification of magnetic fluctuations and their different modes,
- separation of coherent from incoherent processes.

In the following, necessarily incomplete sections, we shall provide a presentation of the polarization dependence of neutron cross-sections and show how the different scattering processes can influence the polarization of the neutron beams. We will then explain how polarized neutron beams can be produced and the polarization determined after scattering. Finally we shall give examples, where the technique of polarized neutron scattering can provide new insight into physical processes in condensed matter research. For a more detailed introduction into the field of polarized neutron scattering with refer the interested reader to the book of Williams [6].

## 2 Elastic neutron scattering cross-section for polarized neutrons

The theory of elastic neutron scattering taking into account polarization effects has been derived by Blume in 1963 [7]. The complete description of the scattering process involving both nuclear and magnetic interactions can be given by means of two master equations. The first one gives the total neutron cross-section which depends on the polarization  $\mathbf{P}_i$  of the incident neutron beam as follows:

$$\sigma = NN^* + \mathbf{D}_\perp \cdot \mathbf{D}_\perp^* + \mathbf{P}_i(\mathbf{D}_\perp N^* + \mathbf{D}_\perp^* N) + i\mathbf{P}_i(\mathbf{D}_\perp^* \times \mathbf{D}_\perp), \quad (4)$$

where  $\sigma$  is the total cross section expressed in  $[\text{cm}^2]$ . For simplicity, the contribution of the nuclear spins is neglected.  $N = N(\mathbf{Q}) = \sum_i b_i \exp(i\mathbf{Q} \cdot \mathbf{r}_i)$  is the structure factor of the atomic structure that depends on the scattering vector  $\mathbf{Q}$  and the scattering lengths of the individual nuclei  $b_i$ ;  $\mathbf{D}_\perp$  is the magnetic interaction vector with  $\mathbf{D}_\perp = \mathbf{D}_\perp(\mathbf{Q}) = \hat{Q} \times (\rho(\mathbf{Q}) \times \hat{Q})$ .  $\rho(\mathbf{Q})$  is the Fourier transform of the magnetic moment distribution and  $\hat{Q} = \mathbf{Q}/|\mathbf{Q}|$ . Therefore, only magnetic components perpendicular to the scattering vector participate in the scattering process. The scalar of the polarization vector  $\mathbf{P}_i$  reflects the degree of polarization of the neutrons, being equal to  $\pm 1$  for a fully polarized beam.

Eq. 4 shows that the neutron cross-section depends only on the square of the chemical and magnetic structure factor if a non-polarized neutron beam ( $\mathbf{P}_i = 0$ ) is used. For a fully

polarized beam ( $|\mathbf{P}_i| = 1$ ), two additional terms contribute to the scattering, namely the *magnetic-nuclear interference* term and the *chiral* term, respectively. The magnetic-nuclear interference term being proportional to  $\mathbf{D}_\perp N^* + \mathbf{D}_\perp^* N$  yields only a non-vanishing contribution to the neutron cross-section if a Bragg reflection is due to nuclear and magnetic scattering, like in ferromagnets and in non-centrosymmetric antiferromagnets with propagation vector  $\mathbf{Q}_0 = 0$ . The chiral term  $\mathbf{D}_\perp^* \times \mathbf{D}_\perp$  is non-zero whenever  $\mathbf{D}_\perp$  is not parallel to  $\mathbf{D}_\perp^*$ , as it is the case e.g. for a helicoidal magnetic structure.

The second master equation provides the polarization of the neutron beam *after* the scattering process relative to the polarization of the incident neutron beam:

$$\begin{aligned} \mathbf{P}_f \sigma &= \mathbf{P}_i N N^* \\ &+ (-1) \mathbf{P}_i (\mathbf{D}_\perp \cdot \mathbf{D}_\perp^*) + \mathbf{D}_\perp (\mathbf{P}_i \cdot \mathbf{D}_\perp^*) + \mathbf{D}_\perp^* (\mathbf{P}_i \cdot \mathbf{D}_\perp) \\ &+ \mathbf{D}_\perp N^* + \mathbf{D}_\perp^* N + i(\mathbf{D}_\perp N^* - \mathbf{D}_\perp^* N) \times \mathbf{P}_i \\ &+ i \mathbf{D}_\perp \times \mathbf{D}_\perp^*, \end{aligned} \quad (5)$$

where  $\mathbf{P}_f$  is the polarization vector of the scattered neutrons. On the one hand, Eq. 5 shows that pure nuclear scattering ( $\mathbf{D}_\perp = 0$ ) leaves the polarization of the neutron beam unchanged. On the other hand, polarisation of the scattered beam is obtained either, as we will see in the next chapter, by scattering neutrons on mixed nuclear-magnetic Bragg reflections or from a helicoidal magnetic structure. In the latter case, with  $\mathbf{D}_\perp N^* + \mathbf{D}_\perp^* N = 0$ , a polarized beam with a polarization given by

$$\mathbf{P}_f = \frac{i \mathbf{D}_\perp \times \mathbf{D}_\perp^*}{\sigma} = \frac{i \mathbf{D}_\perp \times \mathbf{D}_\perp^*}{\mathbf{D}_\perp \cdot \mathbf{D}_\perp^*} \quad (6)$$

is created. We point out that a measurement of the chiral term provides the helicity of a helicoidal magnetic structure as has been shown by Shirane et al. [8]. In the general case, the polarization vector of the neutron beam after scattering is rotated with respect to  $\mathbf{P}_i$  and its length is not necessarily equal to  $|\mathbf{P}_i|$ . The term “*polarization analysis*” therefore refers to the determination of the direction and length of  $\mathbf{P}_f$ .

### 3 Production of polarized neutrons

For a measurement of the polarization dependence of cross sections various techniques to produce and analyze polarized neutron beams have been developed. Depending on the required phase space properties of the beams, i.e. continuous vs. pulsed, energy, divergence, type of detector, etc., different methods for the spin analysis are used. The most common methods are diffraction from single-crystal polarizers (mostly Heusler), reflection from magnetized thin film multi-layers or supermirrors, and absorption of the non-wanted spin state by means of polarized  $^3\text{He}$ . A recent review of these techniques can be found in Ref. [9].

#### 3.1 Single-crystal polarizers

This method produces a polarised neutron beam by taking advantage of the magnetic-nuclear interference term in Eq. 4 and Eq. 5. If a magnetic field is applied to a centro-symmetric crystal

so that all the magnetic moments are saturated and aligned perpendicular to the scattering vector  $\mathbf{Q}$ , the neutron scattering cross-section for Bragg scattering is given by (set  $\mathbf{P}_i = 0$  and  $\mathbf{D}_\perp = \mathbf{D}_\perp^*$  in Eq. 4)

$$\sigma = N^2 + D_\perp^2. \quad (7)$$

The second master equation, Eq. 5, yields for  $\mathbf{P}_i = 0$

$$\mathbf{P}_f = \frac{2N\mathbf{D}_\perp}{\sigma} = \frac{2N\mathbf{D}_\perp}{N^2 + D_\perp^2}. \quad (8)$$

Hence, the diffracted beam from a single-crystal is completely polarized if there is a Bragg reflection with  $|\mathbf{D}_\perp| = |N|$ . Typical examples are the (111) reflection of Heusler  $\text{Cu}_2\text{MnAl}$  ( $d$ -spacing 3.43 Å) and the (200) reflection of the alloy  $\text{Co}_{0.92}\text{Fe}_{0.08}$  ( $d$ -spacing 1.76 Å). Other single crystals like  $\text{Fe}_3\text{O}_4$  or  $\text{Fe}_3\text{Si}$  have also been considered but are less used. All these crystals can be used to produce polarized and monochromatic neutron beams and to analyze the energy and polarization of neutron beams. Therefore, single-crystal polarizers are used for single-crystal diffractometers and in triple-axis spectroscopy. Depending on the requirements on neutron energy and resolution, different  $d$ -spacings must be considered. Recently, the quality and the reflectivity of Heusler monochromators has been improved considerably [10] that will allow to use these crystals at relatively short neutron wavelengths.

### 3.2 Thin films

Total reflection from magnetized thin films can be used to produce polarized neutrons. The angle of total reflection for a ferromagnetic film is given by

$$\theta_c^\pm = \lambda \sqrt{N(b \pm p)/\pi}, \quad (9)$$

where  $\lambda$  is the neutron wavelength.  $N$  is the nuclear density, and  $b$  and  $p$  the nuclear and magnetic scattering lengths, respectively. Thus, by an appropriate choice of materials, a polarized beam can be produced by total reflection. For the special case  $b = p$  all reflected neutrons are polarized. Unfortunately, the reflection angles are only reasonably large for cold neutrons: For example,  $\text{Fe}_{50}\text{Co}_{48}\text{V}_2$  has  $b \simeq p$  and  $\theta_c \simeq 0.4^\circ$  for  $\lambda \simeq 4$  Å [11].

The angles of reflection can be significantly improved by adding artificial magnetic and non-magnetic layers that reflect neutrons at small angles above  $\theta_c$ . Such artificial multi-layers (supermirrors) have been produced by physical vapor deposition by Mezei for the first time [12]. Typical materials combinations are Co/Ti, Fe/Si, and  $\text{Fe}_{50}\text{Co}_{48}\text{V}_2/\text{TiNi}_x$  [9, 13, 14, 15, 16]. The latter combination exhibits a remanent magnetization and can therefore be used as a spin selective device, where no spin flipper is necessary anymore [17]. Recently, the number of layers has been increased steadily thus leading to reflection angles for polarized neutrons of the order of  $0.3^\circ$  for  $\lambda \simeq 1$  Å. These modern devices can now also be used as white beam polarizers for thermal neutrons.

### 3.3 Spin filters

A major drawback of polarizing single-crystals and thin films is their decreasing efficiency with increasing neutron energy, i.e. short wavelength, and the small divergence that they accept (see

Table 1). On the other hand they are maintenance free and easy to use. Therefore, polarizing filters with broad-band characteristics and minor restrictions on divergence are of significant interest for neutron scattering in particular for pulsed spallation sources and spectrometers with large area-detectors.

Table 1: Performance and applications of various neutron polarizers. The quoted values are only approximate. The notation is TAS: triple-axis spectrometer, DAX: double axis diffractometer, NSE: neutron-spin-echo, REF: reflectometer, TOF: time-of-flight, SANS: small angle neutron scattering. The quality factor is defined by  $Q = TP^2$ , where the transmission/reflection  $T$  and polarization  $P$  are taken from the literature.

technique	beam	$E$ -range (meV)	instruments	$T$	$P$	$Q$	ref.
Heusler	fixed $\lambda$	$E < 80$	TAS,DAX	0.62	0.95	0.56	[10]
super-mirror	white	$E < 20$	NSE, TAS, REF, TOF	0.9	0.95	0.81	[15]
$^3\text{He}$	white	$E < 2000$	DAX, TAS, TOF, SANS	0.4	0.80	0.26	[18]
p targets	white	$E \gg 2000$	SANS	0.4	0.80	0.26	[18]
$\text{SmCo}_5$	white	$20 < E < 180$	not implemented	0.3	0.75	0.17	[19]

Whereas Heusler and supermirrors are well established but still progressing techniques, the  $^3\text{He}$  spin filters using direct optical pumping of meta-stable  $^3\text{He}$  [20] have improved during the last few years [18]. The basic idea behind the filter-technique is the polarization dependence of the transmission that can be written in its most simple form as [6]

$$T(\lambda) = \exp(-\sigma_0 Nd) \cosh(\sigma_p Nd), \quad (10)$$

where  $\lambda$  is the neutron wavelength,  $d$  the thickness of the filter and  $N$  the  $^3\text{He}$  density.  $\sigma_0$  and  $\sigma_p$  are the spin-independent and polarization dependent cross-sections of  $^3\text{He}$ , respectively. If the filter is not perfectly polarized, a significant portion of the correctly polarized neutrons will be absorbed. Because the absorption increases with increasing  $\lambda$ , the thickness  $d$  of the filter must be optimized for the wavelength band to be used even if  $\sigma_0$  is small.

$^3\text{He}$  filters are now in regular use at the ILL on several instruments. Due to wall relaxation of polarized He nuclei, the polarization and transmission of the filters decreases with time and they have to be exchanged almost daily. It is foreseen that  $^3\text{He}$  filters will further improve and find applications in particular at pulsed neutron sources and instruments with large area detectors. The method of using spin exchange of  $^3\text{He}$  with optically pumped Rb vapor [21] is progressing too and may challenge the meta-stable type of pumping. One major advantage of the latter technique is that the filter has not to be exchanged during an experiment.

The development of  $\text{SmCo}_5$  polarizing filters has been conducted at ISIS. If the problems of depolarization of the neutrons within the filter and of  $\gamma$ -heating in intense neutron beams can be solved one may obtain a quality factor of  $Q \simeq 0.25$  [19] that is lower than the maximum to be achieved for a future  $^3\text{He}$  filter.

Polarized hydrogen can also be used as polarizing filter. Moreover, the spin dependent interaction of the neutrons with the protons can be used for contrast variation of hydrogen-containing materials in small angle neutron scattering experiments [22]. We defer the interested reader to the literature.

## 4 Determination of Form Factors and Spin Densities

Polarized neutrons allow to measure magnetic densities with improved accuracy as compared to standard diffraction methods. The method presented below applies to magnetic structures described by a propagation vector  $\mathbf{Q}_0 = 0$ . For a paramagnet, a ferromagnetic component can be induced by applying an external magnetic field. According to Eq. 4 in the case of mixed nuclear-magnetic Bragg reflections with real structure factors, the intensity ratio  $R$  of scattered neutrons polarized by an external magnetic field along the  $+z$  or  $-z$  direction, where  $z$  is perpendicular to the scattering plane (that contains  $\mathbf{Q}$ ), is given by

$$R = \frac{I^{+z}}{I^{-z}} = \frac{N^2 + 2ND_{\perp}^z + D_{\perp}^{z2}}{N^2 - 2ND_{\perp}^z + D_{\perp}^{z2}} = \frac{(N + D_{\perp}^z)^2}{(N - D_{\perp}^z)^2}. \quad (11)$$

$D_{\perp}^z$  is the projection of the magnetic interaction vector  $\mathbf{D}_{\perp}$  along the  $z$ -axis. Determination of a spin density with polarized neutrons consists of measuring  $R$  at many different Bragg reflections ( $hkl$ ). As the crystal structure and hence the chemical structure factors  $N$  are presumably known ( $N$  depends on the Miller indices), the method provides usually directly the values of the magnetic structure factors. For small magnetic amplitudes, polarized neutrons give an enhanced sensitivity compared to unpolarized neutrons that yield an intensity  $I_{np} = N^2 + \frac{2}{3}D_{\perp}^2$ . The factor  $2/3$  comes from the spherical averaging of  $\mathbf{D}_{\perp}$  in the second term of Eq. 4 over all directions with respect to  $\mathbf{Q}$  for a non-magnetized isotropic sample.

Namely, considering a typical example with  $D_{\perp} = 0.1N$  yields  $I_{np} \simeq 1.01N^2$ , while the contrast as measured with polarized neutrons,  $R = 1.21N^2/0.81N^2 = 1.49$ , is rather large. Therefore polarized neutrons are particularly well suited for measuring maps in compounds with small magnetic moments (example: heavy fermion systems) or with seriously diluted magnetic moments (example: molecular magnetic crystals).

To extract the magnetic moment density from the data, a classical Fourier calculation is usually performed [23]. Because

$$\rho(\mathbf{Q}) = \int \int \int m(\mathbf{r}) \exp(i\mathbf{Q} \cdot \mathbf{r}) d^3\mathbf{r}, \quad (12)$$

one can obtain the spin density  $m(\mathbf{r})$  in real space by the inverse Fourier transform through the relation

$$m(\mathbf{r}) = \frac{1}{V} \sum_{\mathbf{Q}} \rho(\mathbf{Q}) \exp(-i\mathbf{Q} \cdot \mathbf{r}). \quad (13)$$

As the cloud of unpaired electrons that are responsible for magnetism is extended in real space, the magnetic form factor decreases with increasing  $\mathbf{Q}$  and equivalently with increasing Bragg indices ( $hkl$ ). To obtain precise measurements, data are to be taken up to large values of scattering vectors  $\mathbf{Q}$ . To that end short-wavelength neutrons are to be preferred, and instruments dedicated to such measurements provide usually hot neutrons, like the 2-axis diffractometers D3 at the ILL and 5C1 at the LLB. The layout of such an instrument is presented in Fig. 1. Until now, no polarized neutron diffractometers have been built at a spallation source. In any case, however, the data set is restricted to finite values of  $h$ ,  $k$ ,  $l$ , which leads to oscillatory distortions in the spin density maps  $m(\mathbf{r})$  due to finite size effects [23]. Therefore, other reconstruction methods of the spin density map have been developed. The two most often used techniques are either based on information theory like the maximum entropy method [24] or on the multi-polar expansion of the electronic density [25]. The latter method models the spin



density by a set of parameters that have to be determined by standard least-square fitting calculations.

Figure 1: Schematic arrangement of a two-axis spectrometer used for the determination of magnetic densities. The monochromator produces a polarized beam with the neutron polarization perpendicular to the scattering plane. A small guide field prevents the neutron beam to depolarize. A *spin-flipper* allows to reverse the neutron polarization by  $180^\circ$  and hence to measure the flipping ratio  $R$ . A magnetic field saturates the magnetic moments of the sample along the neutron polarization.

## 4.1 Magnetic Form Factors

Ever since the experiments of Shull and coworkers in the 1960's in 3d ferromagnets [26], the main motivation to measure spin densities has been to gain a better insight in electronic distributions in solid-state materials. Since that time, measurements have been extended to paramagnetic metals and to the 4f-electrons in rare-earth compounds [27, 28].

In 3d-ferromagnets whereas the atomic form factor can be very precisely reproduced from spin-polarized Hartree-Fock calculations [29], there is a strong indication from form factor measurements of a negative spin polarisation between the atomic sites in both Fe and Co. Also, the magnetic moment density-map in Ni [30] and Pd [31] shows an aspherical d-electron distribution plus an orbital contribution. In order to allow for these effects, the form factor is usually written as

$$f(\mathbf{Q}) = \frac{2}{g}(1 + \alpha) \left[ \langle j_0 \rangle + \left( \frac{5}{2}\gamma - 1 \right) A_{hkl} \langle j_4 \rangle \right] + \left[ \frac{(g-2)}{g} f_{orb} - \left( \frac{2}{g} \right) \alpha \delta(\mathbf{Q}) \right], \quad (14)$$

where  $g$  is the Landé factor;  $\alpha$  is a parameter describing the fraction of negative spin polarization;  $\gamma$  is the percentage of electrons in  $E_g$  orbitals which takes into account the orbital contribution [30].  $A_{hkl}$  is a geometrical factor;  $\langle j_0 \rangle$  and  $\langle j_4 \rangle$  represent the spherical and aspherical part of the form factor, respectively. A comparison of the calculated and measured form factors for Ni yielding a uniform negative contribution equal to  $-0.0091\mu_B/\text{\AA}^3$  is shown in Fig. 2. The spin magnetic moment per Ni-atom is  $\mu_{spin} = 0.656\mu_B$  and the orbital contribution  $\mu_{orbital} = 0.055\mu_B$ .

Figure 2: Magnetic moment distribution of Ni in the [100] plane (taken from Ref. [30]).

On the contrary to metallic compounds with  $d$ -electrons,  $f$ -electrons are well localised around the nuclei which allows to perform atomic calculations to obtain the spin distribution. As the orbital moment is usually different from zero, there is an significant contribution of the orbitals to the magnetic density. Also, the spin-orbit coupling is important which results in a mixing of the atomic wave functions. The form factors for the atoms of the rare-earth and actinide series have been calculated by Desclaux and Freeman [32] using the relativistic Dirac-Fock theory. It was shown that the atomic form factor can be expressed as

$$f(\mathbf{Q}) = \langle j_0 \rangle + c_2 \langle j_2 \rangle + c_4 \langle j_4 \rangle + c_6 \langle j_6 \rangle, \quad (15)$$

where

$$\langle j_l(\mathbf{Q}) \rangle = \int_0^\infty U^2(r) j_l(Qr) 4\pi^2 dr. \quad (16)$$

$U(r)$  is the radial wave-function for the unpaired electrons in the atom, and  $j_l(Qr)$  the Bessel function of  $l$ th-order. The coefficients  $c_i$  are tabulated in e.g. Ref. [33].

Among the rare-earth elements, Samarium represents a particular case as the orbital and spin contributions to the magnetisation almost cancel out so that the magnetic density map contains both positive and negative regions. This leads to a form factor which has a maximum located at a position different from  $Q = 0$ . The Sm form factor measured in  $\text{SmCo}_5$  is shown in Fig. 3. An interesting effect is, that as the first excited crystal-field states are located at relative low energies, they become populated when the temperature approaches 300 K. Consequently, the magnetic moment of Sm is only  $\mu \sim 0.04\mu_B$  at room temperature and increases to  $\mu \sim 0.38\mu_B$  for  $T = 4.2$  K [34]. For all temperatures, however, the form factor of Sm has a strong orbital character.

Figure 3: a) Experimental form factor for Sm at  $T = 4.2$  K. The line corresponds to a calculation including crystal field, exchange and spin-orbit effects. b) Same for  $T = 300$  K (taken from Ref. [34]).

Finally, we should point out that a study of the spatial distribution and temperature dependence of the spin density allows to probe the spin susceptibility  $\chi(\mathbf{Q}, 0)$ . As such the method can be used to investigate the nature of the electrons *e.g.* in superconductors. For example, in  $\text{V}_3\text{Si}$  [35] it was shown that the spin susceptibility of the V electrons disappears upon entering the superconducting phase which is an indication of spin-pairing. On the other hand, no similar effect could be observed in the new heavy-fermion superconductors  $\text{UPt}_3$ ,  $\text{UBe}_{13}$  and  $\text{CeCu}_2\text{Si}_2$ . For the latter compounds, the spin susceptibility is temperature independent in the superconducting phase [36]. These results are of particular importance as they impose severe restrictions on the possible pairing mechanisms that can give rise to the electron pairing in these unconventional heavy-fermion superconductors.

## 4.2 Magnetisation distribution in molecular magnets

Molecular magnetism is a fast growing field in material science with potential important technological applications in electronic devices. By building blocks of molecules which contain magnetic centres, magnetic interactions can be tuned and the aim is to synthesize organic compounds which exhibit magnetic ordering at room temperature. To that end, as the number of combinations offered by organic chemistry is almost infinite, it is essential that the mechanism of magnetic couplings originating from  $2p$  electrons to be well understood [37].

In contrast to ionic systems where the electrons which carry magnetism are well localised around the nuclei, the magnetic density of organic compounds is distributed over all molecules due to covalency effects. The effect of delocalisation is even more pronounced when there is no magnetic ion in the molecule and magnetism is due to  $2p$  electrons only [38]. Polarised neutron diffraction yields directly the distribution of electrons responsible for magnetism in organic materials which in turn can be directly compared to theoretical calculations for the electronic

wave-functions and the chemical bonds [39]. Spin density in molecular compounds can also be used to trace exchange pathways through the molecules, like when spin polarisation is found on atoms which in principle are non-magnetic. This is for example the case in the free radical nitronyl nitroxides NitPy(C $\equiv$ C-H). NitPy(C $\equiv$ C-H) builds zig-zag chains linked by C $\equiv$ C-H $\cdots$ O pieces where the hydrogen bridge two molecules. Significant spin population is found at the hydrogen positions ( $\mu \sim 0.04\mu_B$ ) which indicates that the hydrogen bond is involved in the ferromagnetic exchange interactions between the molecules [40].

Figure 4: Spin density projection in NitPy(C $\equiv$ C-H). The contour step for the pyridine cycle is  $0.008\mu_B/\text{\AA}^2$  whereas for the Nit cycle a step is equal to  $0.04\mu_B/\text{\AA}^2$  (taken from Ref. [40]).

A typical example of *spin delocalisation* is found in the compound MnCu(pba)(H<sub>2</sub>O)<sub>3</sub> · 2H<sub>2</sub>O, with pba=1,3-propylenebis(oxamato). The Mn<sup>2+</sup> and Cu<sup>2+</sup> ions are connected by oxamato bridges and build ferrimagnetic chains. The Mn<sup>2+</sup> ions carry a spin  $S_{\text{Mn}} = \frac{5}{2}$  and the Cu<sup>2+</sup> have an effective spin  $S_{\text{Cu}} = \frac{1}{2}$ . Therefore we have the situation where two magnetic metals are linked by organic species. The magnetisation, as obtained from polarised neutron diffraction [41, 44], shows a positive spin population (i.e. the induced magnetisation is aligned along the applied magnetic field) for the Mn spins whereas it is negative for the copper magnetic moments. This reveals the antiferromagnetic nature of the intra-chain coupling. Interestingly, an important contribution to the spin density map is found on the neighboring oxygen and nitrogen ions and on the two central carbon atoms. Summing up the positive and negative spin polarisations individually, one obtains  $5.1\mu_B$  and  $-1.0\mu_B$ , respectively, which shows that the metallic ions have distributed their spin densities on the molecule. The magnetic moments distribution for MnCu(pba)(H<sub>2</sub>O)<sub>3</sub> · 2H<sub>2</sub>O is shown in Fig. 5.

Figure 5: a) Experimental spin density map of MnCu(pba)(H<sub>2</sub>O)<sub>3</sub> · 2H<sub>2</sub>O. The contour step is  $0.005\mu_B/\text{\AA}^2$ . The continuous line represents the positive spin distribution while the dotted line describes the negative magnetisation. b) Calculated spin density map for an isolated molecule with the DMol<sup>3</sup> method (after Ref. [44]). The lowest contour is at  $0.005\mu_B/\text{\AA}^2$ .

Fig. 5 also shows the theoretical spin density for the 'CuMn' molecule projected onto the oxamid mean plane. The theory is based on the local-spin density-functional principles of Perdew and Wang [42]. Calculations for the cation (2+) in vacuum are done with the DMol<sup>3</sup> method [43]. On comparing with experiment it is clear that there is a disagreement with theory on the sign of the spin density at the bridging carbon atoms. One should remember however, that the theory applies to an isolated cation in vacuum. Calculations for smaller than the formal charge reverse the spin density at the bridging carbons. The crystal environment may also change areas with small spin density.

### 4.3 Spin susceptibility in the high- $T_c$ superconductor YBa<sub>2</sub>Cu<sub>3</sub>O<sub>7-x</sub>

The discovery of the high- $T_c$  superconductor La<sub>2-x</sub>Ba<sub>x</sub>CuO<sub>4</sub> with  $T_c = 35\text{K}$  by Bednorz and Müller [45] in 1986 has been at the origin of an enormous amount of work to understand the electronic (charge and spin) correlations in these materials. Following the discovery of the La<sub>2-x</sub>Ba<sub>x</sub>CuO<sub>4</sub> compound, other materials exhibiting similar or higher transition temperatures for superconductivity have been synthesized, like La<sub>2-x</sub>Sr<sub>x</sub>CuO<sub>4</sub>, Nd<sub>2-x</sub>Ce<sub>x</sub>CuO<sub>4</sub>, YBa<sub>2</sub>Cu<sub>3</sub>O<sub>7-x</sub>, and others. All these materials share common features of their crystallographic

structure. They possess  $\text{CuO}_2$ -layers well separated from each other, so that they can be considered as quasi-two-dimensional materials. In this class of materials, superconductivity is achieved by carefully tuning the amount  $x$  of Sr, Ce or O which results in doping the  $\text{CuO}_2$ -layers with charge carriers. The important feature is that the cuprate materials are *either* antiferromagnets and insulators *or* paramagnetic metals and superconductors below a critical temperature  $T_c$ . Important antiferromagnetic correlations and fluctuations persist in the superconducting phase. The role played by these fluctuations in the formation of the superconducting state is still the subject of an intense debate. A central piece of the physics of the high- $T_c$  superconductors is the understanding of the charge and spin states in the  $\text{CuO}_2$ -layers as a function of doping both below and above the transition temperature  $T_c$ .

The intensity of the scattered neutrons can be directly related to the spin susceptibility at  $\mathbf{Q} = 0$  and  $\omega = 0$  through the dissipation-fluctuation theorem. As the signal is particularly small in the high- $T_c$  compounds, use of polarisation analysis is required to enhance the contrast and to isolate the weak magnetic contribution. The results obtained for the temperature variation of the local susceptibility at the copper sites in the  $\text{CuO}_2$  layers is shown in Fig. 6. A particularity of the temperature dependence of the signal is the appearance of the so-called *spin pseudo-gap* in under-doped  $\text{YBa}_2\text{CuO}_{6.52}$  for which the spin susceptibility drops above  $T_c$ . On the other hand, the local spin susceptibility in optimal doped samples decreases only upon cooling below the superconducting temperature [46].

Figure 6: Local spin susceptibility as a function of temperature on copper sites in the  $\text{CuO}_2$  layers in the high- $T_c$  superconductors  $\text{YBa}_2\text{Cu}_3\text{O}_{7-x}$  (taken from Ref. [46]).

## 5 Spherical Neutron Polarimetry

Spherical Neutron Polarimetry (SNP) has recently been developed and successfully tested at the ILL [50] as an alternative way of measuring magnetic structures. Moreover, this method allows to determine form factors and spin densities in antiferromagnets for which very few data is available. The classical technique discussed in chapter 4 cannot be applied in antiferromagnets with propagation vector  $\mathbf{Q}_0 = 0$  when the magnetic and nuclear structure factors are in phase quadrature. For such cases, like  $\text{Cr}_2\text{O}_3$  or even hematite, the neutron cross-section  $\sigma$  is polarisation independent [51]

$$\mathbf{P}_f \sigma = \mathbf{P}_0(1 - \gamma^2) + 2\gamma^2 \hat{\mathbf{Q}}(\mathbf{P}_0 \cdot \hat{\mathbf{Q}}) + 2\gamma(\mathbf{P}_0 \times \hat{\mathbf{Q}}), \quad (17)$$

with  $\sigma = 1 + \gamma^2$  and  $\gamma \hat{\mathbf{Q}} = \Im \mathbf{D}_\perp(\mathbf{Q})/N$ . SNP gives access to the complete set of independent correlation functions involved in the nuclear-magnetic scattering process by a direct measurement of the three components of the polarization vector  $\mathbf{P}_f$  of the scattered neutrons. Eq. 5 shows that if the polarization  $\mathbf{P}_i$  of the incoming neutron beam is fixed, a measurement of  $\mathbf{P}_f$  allows in most cases an unambiguous determination of the direction of the magnetic interaction vector  $\mathbf{D}_\perp$ . This is an alternative way of determining magnetic structure factors to the standard diffraction method that relies on a precise measurement of neutron intensities. Measuring intensities is the same as measuring  $\mathbf{D}_\perp \cdot \mathbf{D}_\perp^*$  which leads to a loss of phase factors and often magnetic structures cannot be unambiguously resolved by unpolarized neutron diffraction. SNP has been successfully applied in problems involving complex magnetic structures, like spiral structures, systems with magnetic domains and small magnetic moments, frustrated antiferromagnets, etc.

It has to be pointed out that the method is sensitive to the direction of the magnetic interaction vector only and not to its magnitude. In this case, finding the value of magnetic moments requires, as usual, the comparison of magnetic and nuclear cross-sections. In contrast to standard single-crystal diffraction, it is insensitive to secondary extinction and allows magnetic structure determination of samples even in the presence of magnetic domains. Namely, magnetic domains depolarize the neutron beam according to their respective population. In other words, the domain population is obtained by measuring the amplitude of the neutron polarization vector  $\mathbf{P}_f$ . In order to perform spherical neutron polarimetry a non-isotropic domain distribution is usually necessary. It can be induced for example by the application of uniaxial pressure.

Spherical neutron polarimetry out-performs standard polarized neutron scattering as it allows to measure both the longitudinal and transverse components of  $\mathbf{P}_f$ . Namely, if a magnetic field is applied to the sample, as it is the case for the longitudinal polarimetry explained in section 4, only the component of the polarization longitudinal to the field can be measured. The transverse components depolarize rapidly and are lost [52]. This is the case in antiferromagnets with mixed nuclear-magnetic Bragg reflections, where most information is contained in the transverse components through the nuclear-magnetic interference term.

## 5.1 Realization of a zero-field chamber: Cryopad

Following the introduction in the previous section it is clear that the transverse components of the polarization can only be measured if the sample is placed in a zero-field chamber. Such a device (called Cryopad) has been constructed at the ILL (Fig. 7) [53]. It consists of two cylindric Meissner shields in the superconducting state. The diameter of the inner shield is large enough to accommodate a cryostat and/or other devices to define the sample environment. Cryopad is centered on the sample table and its orientation is fixed with respect to the wave-vector  $\mathbf{k}_i$  of the incident neutrons. Therefore, the sample can be oriented independently from Cryopad in order to access various Bragg-reflections.

Figure 7: Schematic zero-field chamber *Cryopad II* used for spherical polarimetry at ILL (Taken from Ref. [53]).

The components of the polarization of the incident and scattered neutrons are defined independently by means of two rotating solenoids (called *nutators*) that are placed in the incident and scattered neutron beam. They act as guide-fields in order to orient the neutron polarization vectors  $\mathbf{P}_\alpha$  ( $\alpha = \text{incident, final}$ ) in the plane parallel to the Meissner shields (transverse to  $\mathbf{k}_\alpha$ ). Two spin turning coils between the Meissner shields apply a horizontal field transverse to  $\mathbf{k}_\alpha$  and allow the definition of the component of  $\mathbf{P}_\alpha$  along  $\mathbf{k}_\alpha$ . The modulus of  $\mathbf{P}_f$  is determined by measuring the flipping ratio of the scattered neutrons simply by reversing the field of the nutator after the sample. This can be accomplished quickly by reversing the current in the solenoid. The combined use of the nutators and of the spin turning coils in Cryopad allows the analysis of  $\mathbf{P}_f$  for any direction of  $\mathbf{P}_i$ . In practice, the information is obtained by measuring the three orthogonal components of the final polarization  $P_f^\alpha$  ( $\alpha = x, y, z$ ) for the three orthogonal directions of the initial polarization  $\mathbf{P}_i$ . The direction  $x$  is defined as being along the scattering vector  $\mathbf{Q}$ ,  $z$  is chosen perpendicular to the scattering plane and  $y$  is the last orthogonal direction. For example, if the initial polarization is chosen along the  $z$ -axis, the component of the final polarization along the  $x$ -direction is given by  $P_x = (n_{x+} - n_{x-}) / (n_{x+} + n_{x-})$ , where  $n_{x+}$

and  $n_{x-}$  are the number of neutrons with spins along or anti-parallel to the  $x$ -axis, respectively [53]. Measuring the nine flipping ratios is sufficient to determine the required information about the orientation of the magnetic interaction vector  $\mathbf{D}_\perp(\mathbf{Q})$  and to obtain the value of the ratio between magnetic and nuclear amplitudes  $|\mathbf{D}_\perp(\mathbf{Q})|/N$ . Geometrical relationships between the direction of the final neutron polarization relative to  $\mathbf{P}_i$  have been derived by Nunez *et al.* [54] and are of great help to determine the direction of  $\mathbf{D}_\perp(\mathbf{Q})$ .

## 5.2 Example: UPtGe

Heavy-fermion materials are characterized by a very large linear coefficient of the specific heat and a greatly enhanced Pauli susceptibility, corresponding to effective masses of the quasi-particles of about two orders of magnitude larger than the free electron. Heavy fermions are therefore ideal systems to study strong electron correlations and the number of compounds showing heavy-fermion behavior is large. The ground-state of these systems varies from metallic ( $\text{CeCu}_6$ ,  $\text{CeIn}_3$ ) to insulating ( $\text{Ce}_3\text{Bi}_4\text{Pt}_3$ ) and from antiferromagnetic ( $\text{U}_2\text{Zn}_{17}$ ,  $\text{UPd}_2\text{Al}_3$ ,  $\text{UNi}_2\text{Al}_3$ ) to superconducting ( $\text{UPt}_3$ ,  $\text{UPd}_2\text{Al}_3$ ,  $\text{UNi}_2\text{Al}_3$ ,  $\text{CeCu}_2\text{Si}_2$ ). In most of these systems the magnetic ground state is determined by the competition between the Kondo-effect that tries to screen the magnetic moment and the RKKY interaction that tends to stabilize a ground-state with long-range magnetic order.

Non-collinear magnetic structures in compounds with localized spin-densities can be explained on the basis of the Heisenberg model to originate from competition between exchange forces. In systems with  $5f$ -electrons, like  $\text{U}_3\text{P}_4$  or  $\text{U}_2\text{Pd}_2\text{Sn}$  it has been shown by calculations based on the local-spin density functional theory that a non-collinear arrangement of the magnetic moments is the consequence of strong spin-orbit coupling [55]. However, this theory does not favor the helicoidal-type of magnetic structures found in e.g.  $\text{UNi}_2\text{Al}_3$  and  $\text{UPtGe}$ .

As an example of a magnetic structure determination with the help of spherical neutron polarimetry we show results obtained from the ternary compound  $\text{UPtGe}$  that orders below  $T_N \sim 50$  K with a propagation vector  $\mathbf{Q}_0 = (0.554, 0, 0)$  [56]. Measurements in single crystals using unpolarized neutrons could not decide between an amplitude-modulated spin-density wave and a cycloid with unequal magnetic moments along the  $a$ - and  $c$ -axis (ellipticity), respectively, yielding for the two models similar agreement factors between observed and calculated structure factors [56, 57].

It is seen from Eq. 5 that the direction as well as the amplitude of the polarization of the scattered neutrons depend upon the value of the chiral term. In particular, the chiral component disappears, when  $\mathbf{D}_\perp(\mathbf{Q}_0)$  is parallel to  $\mathbf{D}_\perp^*(\mathbf{Q}_0)$ , as it is the case for an amplitude modulated wave and the polarization of the neutron precesses by  $180^\circ$  around the scattering vector [54]. In contrast, the chiral term gives a contribution to  $\mathbf{P}_f$  if the magnetic structure is a cycloid. Hence, the direction of  $\mathbf{P}_f$  depends on the scattering geometry. Spherical neutron polarimetry therefore allows to distinguish between an amplitude modulated spin-density wave and a helix [59]. For  $\text{UPtGe}$ , the directions of polarization of the diffracted neutrons for directions of  $\mathbf{P}_i$  perpendicular to the scattering plane ( $z$ ), along the scattering vector ( $x$ ), and a third direction in the scattering plane but perpendicular to  $x$  are summarized in table 2. The results of spherical neutron polarimetry unambiguously show that the magnetic structure of  $\text{UPtGe}$  is a cycloid with an axis ratio  $\sim 1.24$  [58], as shown in Fig. 8.

Figure 8: Magnetic structure of UPtGe as determined by spherical neutron polarimetry using the Cryopad device (after [58]).

Table 2: Spherical Neutron Polarimetry data obtained with Cryopad in UPtGe (after Ref. [58]).  $P_i$ ,  $P_f$  and  $P_{calc}$  are the incident, scattered and calculated neutron polarizations. The polarization axis are defined as:  $x$  is parallel to the scattering vector  $\mathbf{Q}$ ;  $y$  is perpendicular to  $\mathbf{Q}$  and in the scattering plane;  $z$  is vertical.

hkl	$P_i$			$P_f$			$P_{calc}$		
	x	y	z	x	y	z	x	y	z
0 <sup>+</sup> 00	0	0	0.9	0.01	-0.05	0.91	0	0	0.90
	0	0.9	0	0.08	-0.91	-0.04	0	-0.90	0
0 <sup>+</sup> 20	0	0	0.9	0.94	-0.11	-0.12	0.97	0	-0.11
	0	0.9	0	0.94	-0.02	0.03	0.97	0.11	0
2 <sup>-</sup> 20	0	0	0.9	-0.91	0	0.16	-0.95	0	0.20
	0	0.9	0	-0.91	-0.10	-0.01	-0.95	-0.2	0
0 <sup>-</sup> 20	0	0	0.9	-0.93	0.05	-0.14	-0.97	0	-0.11
	0	0.9	0	-0.92	0.13	-0.02	-0.97	0.11	0
	0	0	-0.9	-0.92	0.14	0.09	-0.97	0	0.11
	0	-0.9	0	-0.93	0	-0.04	-0.97	-0.11	0

## 6 Inelastic Neutron Scattering with Polarized Neutrons

In analogy to the neutron cross-section derived by Blume [7] for the elastic case, there are three contributions to the inelastic cross section:

- a pure nuclear one that gives rise to phonon scattering,
- a pure magnetic one when neutrons are scattered *e.g.* by spin waves,
- and a magnetic-nuclear interference term that is present only in special cases, as *e.g.* when the spin-lattice interaction in a ferromagnet cannot be neglected.

The inelastic neutron cross-section and its relationship to the neutron polarisation have been derived by many authors (see *e.g.* [1, 60]). In the following we will reproduce the calculations of Maleyev [61] which expresses the time-dependent scattering amplitudes in terms of the Van Hove correlation function

$$\pi S_{AB}(\omega) = \frac{1}{1 - \exp(-\omega/T)} < A, B >''_{\omega}, \quad (18)$$

where  $< A, B >''_{\omega}$  is the absorptive part of the generalised retarded susceptibility

$$< A, B >''_{\omega} = \pi(1 - \exp(-\omega/T))Z^{-1} \sum_{a,b} \exp(-\frac{E_a}{T}) A_{ab} B_{ba} \delta(\omega + E_{ab}). \quad (19)$$

$A$  and  $B$  are operators like  $N(\mathbf{Q})$  or  $\mathbf{D}_{\perp}(\mathbf{Q})$  from Eq. 4;  $Z^{-1}$  is the partition function and  $E_{a,b}$  are the energies between eigenstates of the system. Expressed in such terms, the inelastic

neutron cross-section is given by

$$\sigma = \sigma_n + \sigma_m + \sigma_{nm}, \quad (20)$$

with

$$\begin{aligned} \sigma_n &= \frac{k_f}{k_i} \frac{1}{\pi} \frac{1}{1 - \exp(-\omega/T)} \langle N(-\mathbf{Q}), N(\mathbf{Q}) \rangle''_\omega \\ \sigma_m &= \frac{k_f}{k_i} \frac{1}{\pi} \frac{1}{1 - \exp(-\omega/T)} \sum_{\alpha\beta\gamma} \langle D_\perp^\alpha(-\mathbf{Q}), D_\perp^\beta(\mathbf{Q}) \rangle''_\omega (\delta_{\alpha\beta} + i\epsilon_{\alpha\beta\gamma} P_{i\gamma}) \\ \sigma_{nm} &= \frac{k_f}{k_i} \frac{1}{\pi} \frac{1}{1 - \exp(-\omega/T)} (\langle N(-\mathbf{Q}), \mathbf{D}_\perp(\mathbf{Q}) \rangle''_\omega + \langle \mathbf{D}_\perp(-\mathbf{Q}), N(\mathbf{Q}) \rangle''_\omega) \cdot \mathbf{P}_i. \end{aligned} \quad (21)$$

$\{\alpha, \beta, \gamma\} = \{x, y, z\}$  in Cartesian coordinates. The polarisation vector  $\mathbf{P}_f$  is accordingly given

- for nuclear scattering by  $\mathbf{P}_f \sigma_n = \mathbf{P}_i \sigma_n$ ,
- for pure magnetic scattering by

$$\begin{aligned} P_{f\alpha} \sigma_m &= \sum_{\beta} P_{i\beta} (\langle D_\perp^\alpha(-\mathbf{Q}), D_\perp^\beta(\mathbf{Q}) \rangle''_\omega + \langle D_\perp^\beta(-\mathbf{Q}), D_\perp^\alpha(\mathbf{Q}) \rangle''_\omega) \\ &\quad - \sum_{\beta\gamma} \delta_{\alpha\beta} \langle D_\perp^\gamma(-\mathbf{Q}), D_\perp^\gamma(\mathbf{Q}) \rangle''_\omega - i \sum_{\beta\gamma} \epsilon_{\alpha\beta\gamma} \langle D_\perp^\beta(-\mathbf{Q}), D_\perp^\gamma(\mathbf{Q}) \rangle''_\omega, \end{aligned}$$

- for magnetic-nuclear interference scattering by

$$\begin{aligned} \mathbf{P}_f \sigma_{nm} &= \langle N(-\mathbf{Q}), \mathbf{D}_\perp(\mathbf{Q}) \rangle''_\omega + \langle \mathbf{D}_\perp(-\mathbf{Q}), N(\mathbf{Q}) \rangle''_\omega \\ &\quad + i [\langle N(-\mathbf{Q}), \mathbf{D}_\perp(\mathbf{Q}) \rangle''_\omega - \langle \mathbf{D}_\perp(-\mathbf{Q}), N(\mathbf{Q}) \rangle''_\omega] \times \mathbf{P}_i. \end{aligned}$$

It turns out from these equations that whereas phonons do not change the neutron polarisation, scattering by spin waves do. As we will see below this feature is very useful to separate and identify the different magnetic modes in ferro- and antiferromagnets. For the particular cases of simple ferromagnets and of two-sublattices collinear antiferromagnets, explicit expressions for the polarisation dependence of the inelastic neutron cross-section can be found in the classic paper of Izyumov and Maleev [62]. The magnetic-nuclear interference term gives rise in particular to the so-called *magneto-vibrational* scattering and is also important for a proper understanding of *magneto-elastic* scattering. Their origins are due to the fact that the cloud of electrons that carries magnetism follows the nuclei when they oscillate around their equilibrium position and that the magnetic moment is modulated by the lattice vibrations, respectively. The magneto-vibrational scattering is inelastic in the nuclear system but elastic in the magnetic one. It occurs at the same positions in reciprocal space as the phonons but with a polarisation dependence. It has been exploited *e.g.* to measure the magnetic form factor through the polarisation dependence of phonons at general  $\mathbf{Q}$  positions in Fe [63].

## 6.1 Longitudinal neutron polarimetry

The first spectrometer that allowed the analysis of the scattered neutrons was built by Moon, Riste and Koehler by replacing monochromator and analyzer of a triple-axis spectrometer by



ferromagnetic crystals that were saturated in a magnetic field (Fig. 9) [4]. In contrast to spherical neutron polarimetry the polarization is maintained by means of guide fields throughout the instrument. As a consequence, only the component of the neutron polarization parallel or anti-parallel to the field direction can be measured whereas the transverse components depolarize and are lost. In exactly the same way than the magnetic-nuclear interference term cannot be measured by standard diffraction, the same effect happens for the inelastic counterpart. The magnetic-nuclear interference contribution leads to a rotation of the initial polarisation which averages out if a magnetic field is applied. Such a contribution is only accessible if the sample is enclosed in a zero-field chamber, like the Cryopad device. The standard triple-axis instrument with polarisation analysis developed by Moon et al. allows to measure the energy, momentum and spin dependence of cross sections with the restriction that only longitudinal polarimetry can be performed. In practice, two basic scattering geometries are commonly used: Namely the spin-flip and non spin-flip cross sections are measured with either the polarization of the neutrons parallel or perpendicular to the scattering vector  $\mathbf{Q}$ .

Figure 9: Schematic arrangement of the three axis spectrometer for polarized neutrons used by Moon et al. [4], at Oak Ridge National Laboratory.

An immediate application of longitudinal polarimetry is that for  $\mathbf{P}_i \parallel \mathbf{Q}$  all magnetic scattering involves processes in which the spin of the neutrons is flipped because  $D_{\perp z} = 0$ . We point out again (see Eq. 3) that this is a general rule valid for elastic and inelastic as well as coherent and incoherent scattering. In contrast, if the scattering geometry is chosen such that  $\mathbf{P}_i \perp \mathbf{Q}$  and  $\mathbf{M} \parallel \mathbf{P}_i$  then the elastic magnetic scattering ( $D_x = D_y = 0$ ) is non spin-flip, whereas the inelastic scattering is spin-flip ( $\delta\mathbf{D}_y$ , transverse excitations) and non spin-flip ( $\delta\mathbf{D}_z$ , longitudinal excitations), respectively.

Polarized neutrons in inelastic neutron scattering are often used to separate the magnetic from the nuclear scattering or to distinguish magnetic fluctuations perpendicular and transverse to the magnetization or scattering vector. When scattering by phonons dominates a neutron spectrum an unambiguous determination of the magnetic contribution to the neutron cross-section can be accomplished by measuring the scattering with  $\mathbf{P}_i \parallel \mathbf{Q}$ . A typical example for  $\text{UFe}_2$  is shown in Fig. 10, where the linear dispersion curve of the acoustic phonons can be distinguished from the quadratic dispersion curve of the spin-wave branch in  $\text{UFe}_2$  at low  $T$  in the cross-over regime [64].

Figure 10: Constant-energy inelastic scan in  $\text{UFe}_2$  using polarization analysis showing that spin waves occur in the spin-flip channel (black symbols), while scattering by phonons is non spin-flip (open symbols) (taken from Ref. [64]). The line is simply to guide the eye. See text for details.

Longitudinal polarimetry is not only an important method for measuring magnetic and nuclear cross sections unambiguously, it is also very powerful in separating self and collective dynamics in materials that contain strong incoherent scatterers like hydrogen in biological materials and polymers [65] (see chapter 7).

## 6.2 The XYZ method

The longitudinal polarimetry method can be generalized to polarization analysis along the three Cartesian directions, the so called XYZ method (that is however to be distinguished from spherical polarimetry). This method allows to apply the technique of polarization analysis to time-of-flight spectrometers with multi-detectors. With the coordinate system shown in Fig. 11, the non-spin flip (NSF) and spin-flip (SF) cross-sections are given by [66]

$$\sigma_{NSF}^x = \frac{1}{3}\sigma_{NS} + \frac{1}{2}\sigma_M \sin^2 \alpha + \sigma_N \quad (22)$$

$$\sigma_{NSF}^y = \frac{1}{3}\sigma_{NS} + \frac{1}{2}\sigma_M \cos^2 \alpha + \sigma_N \quad (23)$$

$$\sigma_{NSF}^z = \frac{1}{3}\sigma_{NS} + \frac{1}{2}\sigma_M + \sigma_N \quad (24)$$

$$\sigma_{SF}^x = \frac{2}{3}\sigma_{NS} + \frac{1}{2}\sigma_M(1 + \cos^2 \alpha) \quad (25)$$

$$\sigma_{SF}^y = \frac{2}{3}\sigma_{NS} + \frac{1}{2}\sigma_M(1 + \sin^2 \alpha) \quad (26)$$

$$\sigma_{SF}^z = \frac{2}{3}\sigma_{NS} + \frac{1}{2}\sigma_M. \quad (27)$$

Here,  $\sigma_M$  is the magnetic,  $\sigma_{NS}$  is the nuclear spin incoherent and  $\sigma_N$  is the coherent plus isotopic incoherent nuclear scattering cross-section. The magnetic scattering can be isolated by combining these equations in the following way (independent of the angle  $\alpha$ )

$$\frac{1}{2}\sigma_M = 2\sigma_{NSF}^z - \sigma_{NSF}^y - \sigma_{NSF}^x \quad (28)$$

$$= \sigma_{SF}^x + \sigma_{SF}^y - 2\sigma_{SF}^z. \quad (29)$$

The XYZ-method has been applied successfully in determining the dynamical magnetic response in metals with small magnetic moments like  $V_2O_3$  [67] and in probing both atomic and spin correlations e.g. in spin-glasses [69] or magnetic defects in disordered alloys. A full account of the applicability of the XYZ technique to this problem has been recently reviewed by Cywinski *et al.* [68]. Another important application of the XYZ-method is that it allows to separate incoherent and coherent atomic motions, as presented in chapter 7.

Figure 11: Geometry of the XYZ polarization method.  $\mathbf{P}_i$  and  $\mathbf{P}_f$  are the polarizations of the incident and scattered beams, respectively.  $\mathbf{Q}$  is the scattering vector.

## 6.3 Paramagnetic scattering

According to the Rhodes and Wohlfarth [70] theory, magnetic materials with  $d$ -electrons can be classified in localized and itinerant systems. While for systems with localized spin densities, the magnetic moment in the paramagnetic phase is temperature independent, the ratio between paramagnetic and ordered moments varies with temperature in the Stoner model. The theory of spin fluctuations for localized and itinerant magnetic systems is reasonably well developed in the paramagnetic phase [71]. In that respect, inelastic scattering of neutrons provides direct experimental information on the spectrum of spin fluctuations on an absolute scale as it gives

access to the space- and time-variation of the spin-spin correlation function  $S(\mathbf{Q}, \omega)$  that is related to the imaginary part of the dynamical susceptibility  $\chi(\mathbf{Q}, \omega)$  [1]. Paramagnetic scattering is usually very weak and difficult to separate from coherent (phonons) and incoherent nuclear scattering. However, the signal can be uniquely identified in experiments by using the difference method, namely, the difference between the spin-flip scattering as measured in a (small) field parallel to  $\mathbf{Q}$  and perpendicular to  $\mathbf{Q}$  contains only magnetic scattering [60, 72]. The reason being that, the inelastic scattering from phonons is suppressed and nuclear incoherent scattering as well as room background cancel. This statement is generally valid as long as the nuclear magnetic moments are disordered, i.e.  $\langle I_x^2 \rangle = \langle I_y^2 \rangle = \langle I_z^2 \rangle = \frac{1}{3}I(I+1)$ , and  $\langle I_\alpha \rangle = 0$ . Nuclear ordering occurs only for extremely low temperatures [73].

Therefore one obtains for example

$$\frac{1}{2} \left[ \frac{d^2 \sigma}{d\omega d\Omega} \right]_m = \left[ \frac{d^2 \sigma^{+, -}}{d\omega d\Omega} \right]_{\parallel} - \left[ \frac{d^2 \sigma^{+, -}}{d\omega d\Omega} \right]_{\perp} = \left[ \frac{d^2 \sigma^{+, +}}{d\omega d\Omega} \right]_{\perp} - \left[ \frac{d^2 \sigma^{+, +}}{d\omega d\Omega} \right]_{\parallel}. \quad (30)$$

Once the intensity of the paramagnetic fluctuations is measured, the  $E$ -integrated intensity can be put on an absolute scale by comparison with an acoustic phonon measured close to a Bragg peak [74] or by using an incoherent scatterer like vanadium. Hence, an effective, paramagnetic moment can be found, defined by

$$M(q) = \frac{1}{f(q)} \left[ \int_0^\infty S(q, \omega) d\omega \right]^{1/2}, \quad (31)$$

where  $f(q)$  is the form factor [72]. Ishikawa *et al.* [74] pointed out that Eq. 31 overestimates the amplitude of spin fluctuations at low temperatures when the energy range of the spin fluctuations extends beyond  $\sim k_B T_c$ . They propose instead to use the Kramers-Kronig relation to obtain first the static susceptibility that is linked via the fluctuation-dissipation theorem to the amplitude of the spin fluctuations through  $\langle M^2(q) \rangle = 3k_B T \chi(q)$  for  $\hbar\omega \ll k_B T$  and

$$\chi(q) = g^2 \mu_B^2 \int_{-\infty}^\infty \frac{S(q, \omega) [1 - \exp(-\hbar\omega/k_B T)]}{\hbar\omega} d\omega. \quad (32)$$

Measurements of the paramagnetic fluctuations in MnSi with a coarse energy resolution (so that the  $E$ -integration is automatically performed) with Eq. 31 [72] and Eq. 32 [74] show that the amplitude of the local magnetic moment indeed increases with increasing temperature, in agreement with self-consistent renormalisation theory (Fig. 12) [71].

Figure 12: Temperature dependence of  $4\pi q^2 \langle M_q^2 \rangle$  plotted against  $q$  in MnSi as measured with polarized neutrons by Ishikawa *et al.* [74]. It is apparent from the figure that the mean-square amplitude of the spin fluctuations increases with increasing temperature in agreement with the calculations of the self-consistent renormalisation theory [71].

Using the difference technique, the scaling behavior of many different itinerant ferromagnets has been investigated in the paramagnetic phase and it was shown that the scattering functions of Fe and Ni can be modeled above  $T_C$  by a simple Lorentzian scattering function given by [75]

$$S(q, \omega) = \frac{\omega}{1 - \exp(-\omega/T)} \chi(q=0) \frac{\kappa^2}{\kappa^2 + q^2} \frac{\Gamma_q}{\Gamma_q^2 + \omega^2}, \quad (33)$$

where the inverse correlation length  $\kappa = \kappa_0(T/T_c - 1)^{0.7}$ , the line-width  $\Gamma_q = Aq^{2.5} f(\kappa/q)$ , and  $f(x)$  is approximately given by the Résibois-Piette scaling function [76].

To conclude, polarized neutron scattering is a powerful method to measure paramagnetic fluctuations in particular when the signal is weak.

## 6.4 Transverse and longitudinal excitations in ferromagnets

The magnetic properties of compounds with localized spin densities are usually described by the Heisenberg Hamiltonian

$$H = - \sum_{i,j} J_{ij} \mathbf{S}_i \cdot \mathbf{S}_j \quad (34)$$

where  $J_{ij}$  is the exchange integral between the spins located at the  $i$ - and  $j$ -position, respectively [77]. Depending on the sign of the exchange integral, Eq. 34 favors either antiferromagnetic or ferromagnetic ground-states. If exchange interactions extend beyond nearest neighbors, competing effects can occur that may lead to non-collinear or even incommensurate magnetic structures.

Because of its simplicity, the Heisenberg ferromagnet is often taken as model system to study the properties of phase transitions. Within the simple picture of localized spins, long range order is lost due to the thermal excitation of spin waves that evolve into the critical scattering at  $T_C$ . Using unpolarized neutron scattering the spin dynamics close to  $T_C$  has been investigated in detail [78]. It was shown that the spin waves, i.e. the spin fluctuations transverse to the magnetisation vector  $\mathbf{M}$ , renormalise close to  $T_C$  and that the susceptibility  $\chi(q)$  as measured at small angles diverges at small  $\mathbf{q}$  for  $T \rightarrow T_C$ . Here,  $\mathbf{q}$  is the reduced momentum transfer with respect to the nearest Bragg peak. The divergence of  $\chi(q)$  is due to longitudinal fluctuations along  $\mathbf{M}$  because the cross section for spin waves does not contain a correlation length that diverges at  $T_C$ . Unpolarized neutron scattering was not successful in detecting the longitudinal fluctuations in ferromagnets in contrast to the situation in antiferromagnets [79, 80], where they can be easily observed.

The longitudinal fluctuations can be isolated by means of inelastic neutron scattering with polarization analysis [81]. The experiment is performed by measuring the differential spin-flip and non spin-flip cross sections from a ferromagnetic sample, for example EuS, that is saturated in a vertical magnetic field  $\mathbf{B}_v$  that is perpendicular to the scattering vector  $\mathbf{Q}$ . Fig. 13 shows three typical measurements on EuS that have been performed longitudinal and transverse to the reciprocal lattice point (200) at  $0.93T_C$  [82].

Figure 13: Constant- $Q$  scans probing magnetic fluctuations in the ferromagnetic phase of EuS. The solid lines are fits to the data using Lorentzian spectral weight functions convoluted with the resolution function of the spectrometer IN14 at the ILL. The longitudinal spin waves are reduced in intensity due to the dipolar interactions. The parallel fluctuations are quasielastic.

The spin-flip data shows the spin waves with polarization vectors  $\delta\mathbf{S}$  transverse and parallel to the reduced momentum transfer  $\mathbf{q}$ . The former are the Goldstone modes of the system and diverge like  $\chi_{sw}^T \propto 1/q^2$  (Table 3). The longitudinal spin waves attain a mass [83] due to the dipolar interactions and do not diverge,  $\chi_{sw}^L \propto 1/(q^2 + q_D^2)$ . Finally the non spin-flip data shows the longitudinal fluctuations that are quasielastic and diverge like  $\chi_z \propto 1/(q^2 + \kappa^2)$ . Because the width  $\Gamma_q$  of  $\chi_z(q, \omega)$  is comparable to the spin wave energy  $E_q$  it is clear why the longitudinal fluctuations escaped detection with unpolarized neutron scattering. The results are in qualitative and quantitative agreement with a coupled mode analysis [84] and mode-mode coupling theory [85].

Table 3: Transverse and longitudinal susceptibilities of a Heisenberg ferromagnet with dipolar interactions in the ordered and paramagnetic phases for different directions of the momentum-transfer  $\mathbf{q}$  and accessible by one-dimensional polarization analysis (taken from Ref. [82]).

	$T < T_c$	$T > T_c$
$\mathbf{M} \parallel \mathbf{q}$	$\frac{2}{q^2} + \frac{1}{q^2 + \kappa_z^2 + q_D^2}$	$\frac{2}{q^2 + \kappa^2} + \frac{2}{q^2} + \frac{1}{q^2 + \kappa_z^2 + q_d^2}$
$\mathbf{M} \perp \mathbf{q}$	$\frac{1}{q^2} + \frac{1}{q^2 + q_D^2} + \frac{1}{q^2 + \kappa_z^2}$	$\frac{2}{q^2 + \kappa^2} + \frac{2}{q^2} + \frac{1}{q^2 + \kappa_z^2 + q_d^2}$

## 6.5 Spin waves and phasons in incommensurate, antiferromagnetic Cr

One of the outstanding features of antiferromagnetic Cr is the occurrence of an incommensurate spin-density wave below  $T_N = 311$  K that is transversely polarized ( $\mathbf{S}$  perpendicular  $\mathbf{Q}^\pm$ ) with  $\mathbf{Q}^\pm = (1 \pm \delta, 0, 0)$  being the incommensurate wave-vector [86]. The magnetic excitations exhibit many unusual features that are not well understood. In particular, the magnetic modes that originate from the magnetic satellite peaks at  $\mathbf{Q}^\pm$  have such a steep dispersion that the creation and annihilation peaks cannot be resolved anymore. Using inelastic scattering of unpolarized neutrons and analyzing the width of the peaks in constant energy scans led to the conclusion that the velocity of the excitations is  $c_{sw} \simeq 1020$  meVÅ [87]. This value deviates significantly from the theoretical value of a random phase approximation (RPA) that is given by  $c_{sw}^{th} = \sqrt{\frac{1}{3}}v_F \simeq 1500$  meVÅ, where  $v_F$  is the Fermi velocity [88]. Using unpolarized neutron scattering it has been shown that transverse (with respect to the staggered magnetization) as well as longitudinal excitations contribute to the inelastic scattering that emerges from the incommensurate  $\mathbf{Q}^\pm$  satellite peaks [89].

In the absence of sizable magnetic-nuclear interference contributions in the cross-section, the most direct way to separate the transverse from the longitudinal fluctuations is the use of longitudinal polarimetry. For such an experiment it is necessary to use a Cr single-crystal cooled through  $T_N$  in a large magnetic field in order to induce a single- $\mathbf{Q}$  state. During the experiment, a vertical field  $\mathbf{B} = 4$  T was applied along [001] in order to enforce a single-domain spin density wave with the magnetic moments aligned along the [010] direction. In this configuration, the spin-flip scattering is due to the longitudinal modes and the non spin-flip scattering due to the transverse modes.

Fig. 14 shows constant energy scans for  $E = 4.2$  meV measured in the transverse spin-density-wave phase at  $T = 230$  K ( $0.74T_N$ ) [90]. It is clearly seen that the inelastic, incommensurate peaks with transverse polarization are significantly sharper than the corresponding longitudinal peaks. Therefore, the mode velocity of the spin waves,  $c_{sw}$ , is significantly larger than the mode velocity of the phason modes,  $c_{ph}$ . These results are in qualitative agreement with results of RPA theory [88]. In addition, the data shows that the enhanced magnetic scattering at (100) and  $E = 4.2$  meV has a longitudinal polarization. Without going into further details the results indicate that a proper understanding of the magnetic excitations in Cr can only be gained if polarization analysis is used.

Figure 14: Constant- $E$  scans at 4.2 meV, probing the longitudinal and transverse excitations along the  $[100]$  direction in the transverse spin-density-wave phase of Cr at  $T = 230$  K. The inset shows the intersection of the constant- $E$  scan with the dispersion of the the transverse (solid lines) and the longitudinal modes (broken lines) as well as the Fincher-Burke modes.

## 6.6 Magnetic excitations in a heavy fermion superconductor

The heavy fermion superconductor UPd<sub>2</sub>Al<sub>3</sub> exhibits the unusual coexistence of antiferromagnetism and superconductivity below  $T_c = 2$  K, i.e. the ordered magnetic moments of the  $f$ -electrons of  $U$  persist in the superconducting phase [91]. This has been taken as a sign that the interplay of magnetism and superconductivity could be studied in this material. Neutron [92] and x-ray scattering [93] experiments have shown that the magnetic structure of UPd<sub>2</sub>Al<sub>3</sub> consists of ferromagnetic planes stacked along the  $c$ -axis with a propagation vector  $\mathbf{Q}_0 = (0, 0, 0.5)$ . The magnetic moments are confined within the hexagonal plane and are found to have an unusually large value of  $\mu = 0.85\mu_B$  at saturation. First elastic [94, 95] and inelastic [96] neutron scattering experiments could not unambiguously reveal any change in the magnetic properties of UPd<sub>2</sub>Al<sub>3</sub> upon cooling the sample below the superconducting transition temperature.

Inelastic neutron scattering experiments [97, 98] performed with an improved energy-resolution as compared to the work of Petersen et al. [96] showed that there exist two contributions to the spectrum of magnetic fluctuations in UPd<sub>2</sub>Al<sub>3</sub>. While the first one corresponds to the spin-wave previously measured by Petersen et al. [96], a second mode localized around the antiferromagnetic wave-vector  $\mathbf{Q}_0$  is observed in the energy range  $0 < E < 0.5$  meV. This lower energy mode is heavily damped for all temperatures in the antiferromagnetically ordered phase and strongly sharpens upon passing into the superconducting phase. At the lowest temperature the low-energy mode develops an apparent energy gap with a value comparable to  $T_c$  [98, 99]. Further evidence of a strong interplay between magnetic fluctuations and superconductivity in this compound originates from the use of polarized neutrons as shown in Fig. 15. Using a polarized beam, it was possible to show that the two magnetic modes are both polarized transverse to the magnetization vector and hence are likely to interact with each other [100].

To perform this experiment the sample was field-cooled, so that the magnetic domains could be aligned along the magnetization vector  $\mathbf{M}$ . Using a neutron polarization perpendicular to the scattering plane, it turns out that magnetic fluctuations parallel to the magnetization are non-spin flip, while those perpendicular to  $\mathbf{M}$  appear in the spin-flip channel. Analysis of the line-shape of the inelastic neutron scattering data suggests that  $f$ -electrons located in a small energy range around the Fermi surface play a significant role in forming the superconducting state in UPd<sub>2</sub>Al<sub>3</sub> [101].

Figure 15: Experimental data from UPd<sub>2</sub>Al<sub>3</sub> at the antiferromagnetic wave vector  $\mathbf{Q}_0 = (0, 0, 0.5)$  and  $T = 150$  mK. The data were taken with a fixed outgoing neutron wave vector of  $k_f = 1.15 \text{ \AA}^{-1}$ . Frame a) and b) are taken with polarized neutrons. For means of comparison a scan measured with unpolarized neutrons is shown in frame c). In frame a) and b), the transverse response is shown as black symbols, whereas the longitudinal component is represented by open circles. See Ref. [100] for details.

## 6.7 Magnons and Solitons in low-dimensional systems

The magnetic properties of low-dimensional compounds have attracted a lot of attention as new effects due to quantum fluctuations are strong. For one-dimensional Heisenberg antiferromagnets the ground states and energy excitations are different for integer- and half-integer spins [102]. Antiferromagnetic chains with  $S = 1/2$  spins have a disordered ground-state. The low-lying excitations are characterized by a continuum of excitations without energy gap at the zone center. On the other hand, for integer-spins a finite energy gap was predicted by Haldane and obtained by numerical calculations [102, 103]. Examples of materials exhibiting a Haldane gap are NENP [104],  $\text{Y}_2\text{BaNiO}_5$  [105], or  $\text{CsNiCl}_3$  [106]. The characteristics expected for a Haldane system have been observed in these compounds by inelastic neutron scattering, like i) a periodicity of  $2\pi$  in the magnon dispersion, ii) line-width broadening of the magnetic excitations as a function of momentum transfer indicating the presence of a two-magnon continuum, and iii) a large field dependence of the magnetic excitations [107].

Polarized neutron scattering experiments have shown that the energy gap in the spectrum of magnetic excitations in  $\text{CsNiCl}_3$  is a triplet [108]. In such quasi-one-dimensional antiferromagnets, weak inter-chain exchange interactions  $J'$  can lead to a Néel phase at low temperatures. In fact the ordering temperature depends on the ratio of the intra-chain interactions  $J$  to  $J'$ . Interestingly, for such systems, where antiferromagnetic ordering is close to disorder, linear spin-wave theory does not account properly neither for the energy-dependence of the magnetic excitations nor for the number of magnetic modes. In particular, the existence of a longitudinally polarized magnetic mode that cannot be predicted by standard or modified spin-wave theory has been proven by means of inelastic polarized neutron scattering in  $\text{CsNiCl}_3$  [106] and  $\text{Nd}_2\text{BaNiO}_5$  (Fig. 16) [109]. The instrumental set-up was chosen so that magnetic excitations transverse to the magnetic moments could be separated from the fluctuations along the spin direction. With such a geometry, it could be shown that additional excitations with longitudinal polarization are present in the spectrum of  $S(\mathbf{Q}, \omega)$ , in agreement with calculations based on renormalization-group theory [110].

Figure 16: Temperature dependence of constant Q-scans measured in  $\text{Nd}_2\text{BaNiO}_5$  with polarized neutrons. Open and black circles refer to spin-flip and non spin-flip scattering respectively (Taken from Ref. [109]).

The quasi-one-dimensional  $S = 1/2$  inorganic compound  $\text{CuGeO}_3$  presents the particularity to undergo a chemical phase transition below  $T = 14$  K to a phase, called *Spin-Peierls* phase, where the copper chain is dimerised [111]. Consequently, the exchange interactions along the chain direction are not uniform anymore but alternate with values  $J$  and  $J'$ , respectively. The magneto-elastic interaction is presumably responsible for this phase transition characterized by a non-magnetic ground state. For such a system, the spectrum of magnetic excitations attains a gap at the zone center whereas the first excited states are triplets. In  $\text{CuGeO}_3$  the gap has a value of  $\Delta \sim 2.5$  meV [112] while away from the zone center, the spectrum of magnetic fluctuations is strongly dispersive along the copper chain direction. High-resolution inelastic polarized-neutron experiments, however, revealed that there is a second energy gap in this compound which separates the low-energy magnon-like mode from a continuum of excitations extending to higher energies [113]. The occurrence of two energy gaps in the spectrum of magnetic excitations in  $\text{CuGeO}_3$  is clearly a signature of strong quantum fluctuations in  $S = 1/2$  antiferromagnetic chains. This behavior differs drastically from one-dimensional systems with

large spin number  $S$  that in some cases can be described by the classical sine-Gordon equation. The combined effects of non-linearity and dispersion in these systems lead in addition to the linear excitations to a special class of excitations called 'solitons' [108].

In a ferromagnetic chain, an excitation of soliton-type can be viewed as a  $2\pi$  turn of the spins over a small distance, in a similar way to a domain wall that would propagate through the crystal. These excitations are accessible to inelastic neutron scattering and in particular to polarized neutrons that allow to measure selectively the different space and time correlation functions  $S^{x,x}(\mathbf{Q}, \omega)$ ,  $S^{y,y}(\mathbf{Q}, \omega)$  and  $S^{z,z}(\mathbf{Q}, \omega)$  [108]. Although experiments with unpolarized neutrons have shown strong evidence of non-linear excitations in the chain compounds  $\text{CsNiF}_3$  and TMMC, a crucial test for the existence of solitonic excitations is the measurement of the components fluctuating along and perpendicular to an applied magnetic field [114].

By separating the longitudinal part  $S^{\parallel}(\mathbf{Q}, \omega)$  of the dynamic structure factor from the transverse part  $S^{\perp}(\mathbf{Q}, \omega)$  with longitudinal polarimetry analysis (see Fig. 17), Boucher *et al.* [115] were able to study the wave-vector and energy dependence of solitonic fluctuations in the antiferromagnetic chain compound  $(\text{CD}_3)_4\text{NMnCl}_3$  (TMMC). This study led to the result that amplitude and lifetime of the solitons are strongly affected by collisions with magnons and by mutual interactions. As a consequence, the line shape and the line width of the experimental dynamical susceptibility differ from the actual theoretical calculations based upon the low density non-interacting soliton gas model [108].

Figure 17: Spectra of magnetic excitations measured in TMMC with inelastic polarized neutron scattering showing that the transverse and longitudinal fluctuations are different. See text and Ref. [115] for details.

## 7 Self and collective diffusive atomic motions

Collective motions of light atoms in metals consist of two different processes [116]. The first one can be viewed as pure diffusion of ions through the lattice while the second process involves cooperative hopping of mutually interacting particles. Hence, the neutron scattering functions contain incoherent and coherent scattering contributions that are given within the random phase approximation by Lorentzian functions centered around zero energy transfer

$$\begin{aligned} S_{inc}(Q, \omega) &= \frac{1}{\pi} \frac{D_t Q^2}{(D_t Q^2)^2 + \omega^2} \\ S_{coh}(Q, \omega) &= \frac{S(Q)}{\pi} \frac{D_c Q^2}{(D_c Q^2)^2 + \omega^2}. \end{aligned} \quad (35)$$

$S(Q)$  is the static structure factor and  $D_t$  and  $D_c$  are the coefficients of incoherent and coherent diffusion, respectively.

To separate the two quasi-elastic scattering processes which appear simultaneously in the neutron spectrum, it is best to use polarization analysis. In analogy to paramagnetic scattering, coherent and incoherent processes can be isolated by calculating the difference between non spin-flip and spin-flip scattering. In the case of different isotopes and disordered nuclear spins,



the matrix elements for non spin-flip and spin-flip scattering are given for the coherent cross-section by

$$\sigma_{coherent}^{++} = \sigma^{--} = \langle N \rangle_{iso}^2 \quad (36)$$

$$\sigma_{coherent}^{+-} = \sigma^{-+} = 0 \quad (37)$$

and for the incoherent scattering by [60]

$$\sigma_{incoherent}^{++} = \sigma_{incoherent}^{--} = \langle N^2 \rangle_{iso} - \langle N \rangle_{iso}^2 + \frac{1}{3} \langle B^2 I(I+1) \rangle_{iso} \quad (38)$$

$$\sigma_{incoherent}^{+-} = \sigma_{incoherent}^{-+} = \frac{2}{3} \langle B^2 I(I+1) \rangle_{iso}, \quad (39)$$

where  $\langle \dots \rangle_{iso}$  refers to isotopic averaging and  $I$  to the nuclear spin [60]. In compounds that contain scatterers with one isotope only, the coherent cross-section is obtained by dividing the spin-flip scattering by 2 and subtracting the result from the non-spin flip intensity. In this case, all the incoherent scattering is spin-flip scattering. Fig. 18 shows the results of measurements of the self and collective dynamics of deuterium in a single crystal of Nb using the time-of-flight spectrometer D7 at ILL with the method described in chapter 6.2 [65]. It is clear that polarization analysis gives an unambiguous separation of the incoherent and coherent quasi-elastic signals over a large range of momentum transfers  $\mathbf{Q}$ . Such a study allows to determine distance and direction of jump processes, hopping and residential times through the analysis of the  $\mathbf{Q}$ -dependence and energy width of the Lorentzian functions in Eqs. 35.

Figure 18: Coherent and incoherent scattering processes observed and calculated in  $\alpha'$ -NbD<sub>0.7</sub> by means of polarized neutron scattering on the multi-counter time-of-flight spectrometer D7 at the ILL (taken from Ref. [65]).

## 8 Conclusions

The examples given in the previous chapters have shown that neutron scattering with polarized neutrons has become a very important means to measure magnetic properties over a wide range of  $\mathbf{Q}$  and  $\omega$  and to distinguish between coherent and incoherent excitations in materials. Most experiments with polarized neutrons are being performed up to now at sources providing continuous neutron beams. The main reason being that most neutron polarizers are more ideally suited for applications with constant wavelength. The recent advances in the field of supermirrors and  $^3\text{He}$  filters have improved the situation. The new devices allow to extend polarization analysis to high neutron energies and to use large area detectors. Therefore, we expect that polarization analysis will also soon become a standard technique at pulsed neutron sources.

Recently, new developments in the field of magnetism have emerged that rely strongly on new developments in polarized neutron scattering. As a first example, we mention systems that can be characterized by sets of exponents, that differ according to the space- and spin-dimensionality and hence can be grouped into universality classes. In frustrated spin systems, the order parameter includes a term describing the spin chirality  $\mathbf{C} = [\mathbf{S}_1 \times \mathbf{S}_2]$ . A direct observation of the fluctuations of the chiral variable is, however, impossible with unpolarized neutron scattering as these are related to four-spin correlation functions. Because the chiral part

of the neutron cross-section is polarization dependent [117] it can be observed with polarization analysis.

As a second example, we mention that the Cryopad technique opens the possibility to apply spherical neutron polarimetry in inelastic neutron scattering as it allows to measure the nuclear-magnetic interference term directly. Recently, Maleyev [61] has reconsidered the implication of the nuclear-magnetic interference term (NMIT) for inelastic scattering and has shown that in analogy with elastic scattering, it leads to a dependence of the neutron cross-section upon  $\mathbf{P}_i$ , namely to a finite polarization of the scattered neutrons and to a rotation of the initial polarization. In particular, Maleyev has shown that the part of the dynamical susceptibility due to the NMIT is non-zero if there is a spin-lattice interaction characterized by an axial vector, as it is the case e.g. for the Dzialoshinskii-Moriya (DM) interaction  $\mathbf{D} \cdot [\mathbf{S}_i \times \mathbf{S}_j]$ . Indications of the importance of the DM-interaction in the spin-lattice coupling and hence on its accessibility through inelastic spherical neutron polarimetry originates from recent inelastic experiments performed in the spin-Peierls compound  $\text{CuGeO}_3$  where a rotation of the final polarization  $\mathbf{P}_f$  has been detected when the incident polarization is chosen parallel to the scattering vector [118]. Such measurements have shown that spherical neutron polarimetry can be applied in the field of inelastic neutron scattering, although counting times are long due to poor statistics. A further application may be the study of magneto-elastic coupling that plays an important rôle in invar alloys [119]. Together with new theoretical interest on such problems, it is probable that this method will contribute to an improved understanding of phase transitions, where spin-lattice interactions are important, as such effects cannot be studied by standard polarization analysis.

## References

- [1] S.W. Lovesey in *Theory of Neutron Scattering from Condensed Matter, Vol. 2*, Clarendon Press, Oxford, 1984.
- [2] R. Nathans, C. Shull, G. Shirane, and A. Andresen, *Phys. Chem. Solids* **10**, 138 (1959).
- [3] O. Halpern and M. R. Johnson, *Phys. Rev* **55**, 898 (1939).
- [4] R. M. Moon, T. Riste and W. C. Koehler, *Phys. Rev.* **181**, 920 (1969).
- [5] F. Mezei, *Z. Physik* **255**, 146 (1972).
- [6] W. Gavin Williams in *Polarized Neutrons*, Oxford Science Publications, Clarendon Press, Oxford 1988.
- [7] M. Blume, *Phys. Rev. B* **130**, 1670 (1963).
- [8] G. Shirane, R. Cowley, C. F. Majkrzak, J. B. Sokoloff, B. Pagonis, and C. H. Perry, *Phys. Rev. B* **28**, 6251 (1983).
- [9] I.S. Anderson, B. Hamelin, P. Hoghoj, P. Courtois, and H. Humblot, *Proceedings of the Seventh School on Neutron Scattering, Frontiers of Neutron Scattering*, Ed. Albert Furrer, World Scientific, 44 (2000).
- [10] P. Courtois, *Physica B* **267-268**, 363 (1999).

- [11] O. Schärpf, J. Physics E: Sci. Instrum. **8**, 268 (1975).
- [12] F. Mezei, Commun. Phys. **1**, 81 (1976); F. Mezei and P.A. Dagleish, Commun. Phys. **2**, 41 (1977).
- [13] Th. Krist, D.J. Müller, and F. Mezei, Physica B **267-268**, 194 (1999).
- [14] V.G. Syromyatnikov, A. Menelle, B.P. Toperverg, Z.N. Soroko, and A.F. Schebetov, Physica B **267-268**, 190 (1999).
- [15] P. H Hoghoj, I. Anderson, R. Siebrecht, W. Graf, and K. Ben-Saidane, Physica B **267-268**, 355 (1999).
- [16] S.H. Lee and C.F. Majkrzak, Physica B **267-268**, 341 (1999).
- [17] P. Böni, J. Neutron Research **5**, 63 (1996); P. Böni, D. Clemens, M. Senthil Kumar, and C. Pappas, Physica B **267-268**, 320 (1999).
- [18] W. Heil, J. Dreyer, D. Hoffmann, H. Humblot, E. Lelièvre-Berna and F. Tasset, Physica B **267-268**, 328 (1999).
- [19] J. Mayers, R. Cywinski, I.R. Harris, M. Hixon, W.G. Williams, in *Proc. Ninth Int. Conf. on Advanced Neutron Sources*, ICANS IX, SIN, Villigen, Switzerland (1986).
- [20] F.D. Colgrove, L.D. Schearer, and K. Walker, Phys. Rev. **132**, 2561 (1963).
- [21] M.A. Bouchiat, T.R. Carver, and C.M. Varnum, Phys. Rev. Lett. **5**, 373 (1960).
- [22] H.B. Stuhrmann, Physica B **267-268**, 92 (1999).
- [23] for a recent Review see J. Schweizer, in *Magnetic Neutron Scattering*, Ed. Albert Furrer, World Scientific, 70 (1995).
- [24] R. Papoular, and B. Gillon, Europhys. Lett. **13**, 429 (1990); R. Papoular, and B. Gillon, in *Neutron Scattering Data Analysis*, Ed. M.W. Johnson, Adam Hilger Publisher, 101 (1990).
- [25] B. Gillon, and J. Schweizer, in *Molecules in Physics, Chemistry and Biology*, Vol. 3, Ed. J. Maruani, Kluwer Academic Publishers, 111 (1989).
- [26] C.G. Shull and Y. Yamada, J. Phys. Soc. Japan **17**, Suppl. B-III, 1 (1962); see also R.M. Moon, Phys. Rev. **136** A195 (1964); H.A. Mook, Phys. Rev. **148**, 495 (1966).
- [27] R.M. Moon, J. Physique, Colloque C7, Suppl. 12, **43**, C7-187 (1982) and references therein.
- [28] J.X. Boucherle, D. Givord, and J. Schweizer, J. Physique, Colloque C7, Suppl. 12, **43**, C7-199 (1982) and references therein.
- [29] R.E. Watson and A.J. Freeman, J. Acta Cryst. **14**, 27 (1961).
- [30] H.A. Mook, Phys. Rev. **148**, 495 (1966).
- [31] J.W. Cable, E.O. Wollan, G.P. Felscher, T.O. Brun, and S.P. Hornfeldt, Phys. Rev. Lett. **34**, 278 (1975).
- [32] A.J. Freeman and J.P. Desclaux, J.M.M.M. **12**, 11 (1979).

- [33] P.J. Brown, in *International Tables for Crystallography*, Vol. C, Kluwer Academic Publishers, 391 (1992).
- [34] D. Givord, J. Laforest, J. Schweizer, and F. Tasset, *J. Appl. Phys.* **50**, 2008 (1979).
- [35] C.G. Shull and F.A. Wedgwood, *Phys. Rev. Lett.* **16**, 513 (1966).
- [36] C. Stassis, J. Arthur, C.F. Majkrzak, J.D. Axe, B. Batlogg, J. Remeika, Z. Fisk, J.L. Smith, and A.S. Edelstein, *Phys. Rev. B* **34**, 4382 (1986).
- [37] O. Kahn, in *Molecular Magnetism*, VCH Publishers Inc., 1993.
- [38] J. Schweizer, *Physica B*, **234-236**, 772 (1997).
- [39] E. Ressouche, *Physica B*, **267-268**, 27 (1999).
- [40] Y. Pontillon, E. Ressouche, F. Romero, J. Schweizer, and R. Ziessel, *Physica B*, **234-236**, 788 (1997).
- [41] V. Baron, B. Gillon, O. Kahn, C. Mathonière, M. Bonnet, and J.X. Boucherle, *Mol. Cryst. Liq. Cryst.* **223**, 247 (1993).
- [42] John P. Perdew and Yue Wang, *Phys. Rev. B*, textbf45, 13244 (1992).
- [43] B. Delley, *J. Chem. Phys.*, **1990**, **92**, 508 (1990); B. Delley, *J. Chem. Phys.* **113**, 7756 (2000).
- [44] V. Baron, B. Gillon, O. Plantevin, A. Cousson, C. Mathoniere, O. Kahn, A. Grand, L. Ohrstrom and B. Delley, *J. Am. Chem. Soc.*, **118**, 11822 (1996).
- [45] J.G. Bednorz and K.A. Müller, *Z. Physik B* **64**, 189 (1986).
- [46] J.X. Boucherle, J.Y. Henry, R.J. Rapoular, J. Rossat-Mignod, J. Schweizer, F. Tasset, and G. Uimin, *Physica B*, **192**, 25 (1993); J.Y. Henry, R.J. Rapoular, J. Schweizer, F. Tasset, G. Uimin and I. Zobkalo, *Physica C* **235-240**, 1659 (1994).
- [47] B. Coqblin, J. Arispe, A.K. Bhattacharjee, and S.M.M. Evans, in *Selected Topics in Magnetism*, Ed. L.C. Gupta and M.S. Multani, *Frontiers in Solid State Sciences* Vol. 2, p.75 (1993).
- [48] T. Takabatake, F. Teshima, H. Fujii, S. Nishigori, T. Suzuki, T. Fujita, Y. Yamaguchi, J. Sakurai, and D. Jaccard, *Phys. Rev. B* **41**, 9607 (1990).
- [49] T.J. Hammond, G.A. Gehring, M.B. Suvasini, W.M. Temmerman, *Phys. Rev. B* **51**, 2994 (1995).
- [50] P.J. Brown, J.B. Forsyth, and F. Tasset, *Proc. Roy. Soc. London A* **442**, 147 (1993).
- [51] P.J. Brown, J.B. Forsyth, and F. Tasset, *Physica B*, **267-268**, 215 (1999).
- [52] R.R. Newton, and C. Kittel, *Phys. Rev.* **74**, 1604 (1948).
- [53] F. Tasset, P.J. Brown, E. Lelièvre-Berna, T. Roberts, S. Pujol, J. Allibon, and E. Bourgeat-Lami, *Physica B* **267-268**, 69 (1999).
- [54] V. Nunez, P.J. Brown, J.B. Forsyth, and F. Tasset, *Physica B* **174**, 60 (1991).

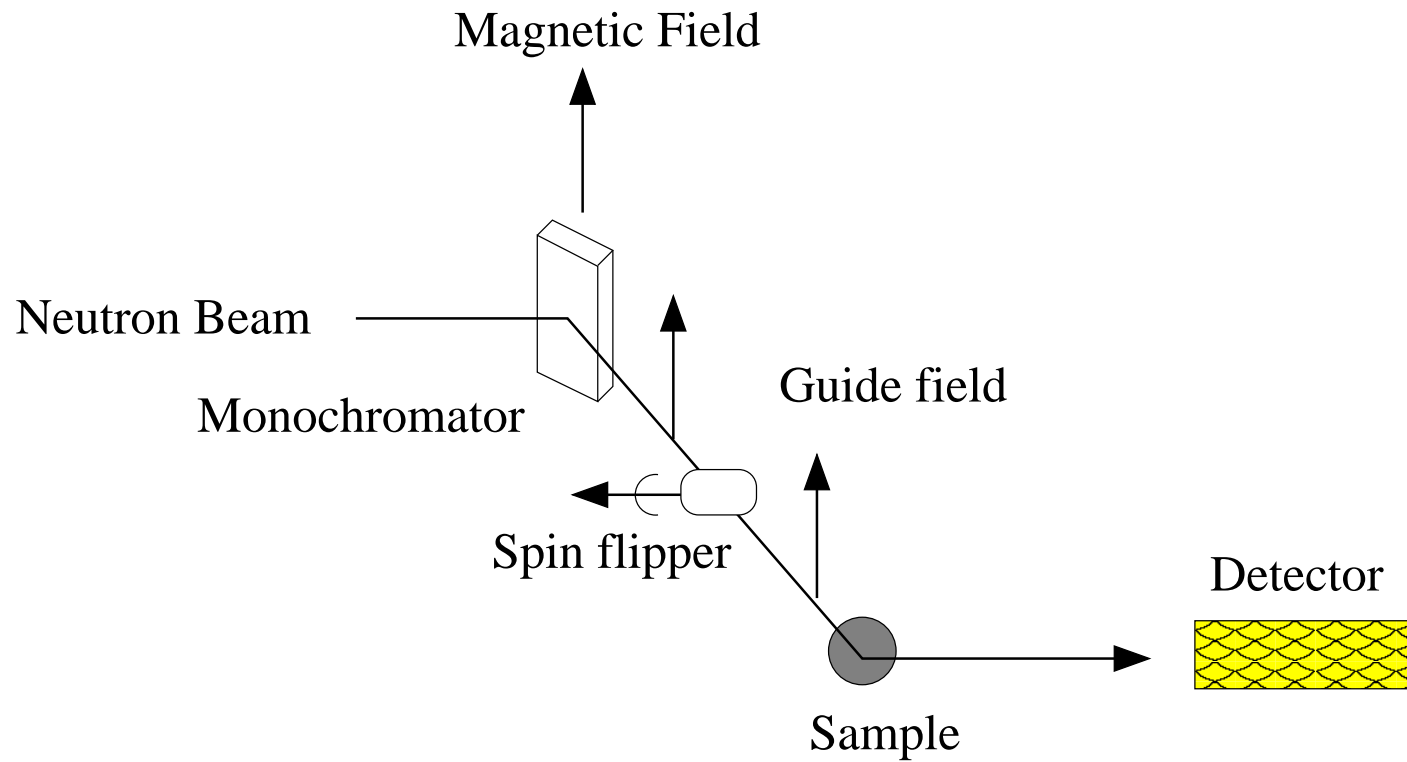
- [55] L.M. Sandratskii, and J. Kübler, Phys. Rev. Lett. **75**, 946 (1995).
- [56] R.A. Robinson, A.C.S. Lawson, J.W. Lynn, and K.H.J. Buschow, Phys. Rev. B **47**, 6138 (1993).
- [57] A. Szytula, M. Kolenda, R. Troc, V.H. Tran, M. Bonet, and J. Rossat-Mignod, Solid State Commun. **81**, 481 (1992).
- [58] D. Mannix, S. Coad, G.H. Lander, J. Rebizant, P.J. Brown, J.A. Paixão, S. Langridge, S. Kawamata, and Y. Yamaguchi, Phys. Rev. B **62**, 3801 (2000).
- [59] J.A. Paixao, M. Ramos Silva, S. Aa. Sorensen, B. Lebech, G.H. Lander, P.J. Brown, S. Langridge, E. Talik, A.P. Goncalves, Phys. Rev. B **61**, 6176 (2000).
- [60] G.L. Squires, *Thermal Neutron Scattering*, Cambridge University Press, Cambridge, 1978.
- [61] S.V. Maleyev, Physica B **267-268**, 236 (1999).
- [62] Yu. A. Izyumov, and S.V. Maleev, Sov. Phys. JETP **14**, 1168 (1962).
- [63] O. Steinsvoll, R.M. Moon, W.C. Koehler, and C.G. Windsor, Phys. Rev. B **24**, 4031 (1981).
- [64] L. Paolasini, G.H. Lander, S.M. Shapiro, R. Caciuffo, B. Lebech, L.P. Regnault, B. Roessli, J.M. Fournier, Europhys. Lett. **34**, 459 (1996).
- [65] J.C. Cook, D. Richter, O. Schärpf, M.J. Benham, D.K. Ross, R. Hempelmann, I.S. Anderson, and S.K. Sinha, J. Phys.: Condens. Matter **2**, 79 (1990).
- [66] O. Schärpf and H. Capellmann, Phys. Stat. Solidi A **135**, 359 (1993).
- [67] J.W. Taylor, T.J. Smith, K.H. Anderson, H. Capellmann, R.K. Kremer, A. Simon, O. Schärpf, K.U. Neumann, and K.R.A. Ziebeck, Eur. Phys. J. B **12**, 199 (1999).
- [68] R. Cywinski, S.H. Kilcoyne, and J.R. Stewart, Physica B, **267-268**, 106 (1999) and references therein.
- [69] A.P. Murani, O. Schärpf, K.H. Andersen, D. Richard, R. Raphael, Physica B **267-268**, 131 (1999).
- [70] P. Rhodes and E.P. Wohlfarth, Proc. R. Soc. A **273**, 247 (1963).
- [71] T. Moriya, in *Spin Fluctuations in Itinerant Electron Magnetism*, Springer Verlag, 1985.
- [72] K.R.A. Ziebeck and P.J. Brown, J. Phys. F: Metal Phys. **10**, 2015 (1980).
- [73] K. Siemensmeyer, K. N. Clausen, K. Lefmann, O. V. Lounasmaa, A. Metz, K. K. Nummila, F. B. Rasmussen, M. Steiner, J. T. Tuoriniemi, and R. T. Vuorinen, Physica B **234-236**, 768 (1997).
- [74] Y. Ishikawa, Y. Noda, Y.J. Uemura, C.F. Majkrzak, and G. Shirane, Phys. Rev. B **31**, 5884 (1985).
- [75] J.P. Wicksted, P. Böni, and G. Shirane, Phys. Rev. B **30**, 3655 (1984).
- [76] R. Résibois and C. Piette, Phys. Rev. Lett. **24**, 514 (1970).

- [77] P. Fazekas, in *Lectures Notes on Electron Correlations and Magnetism*, Series in Modern Condensed Matter Physics, Vol. **5** (1999).
- [78] L. Passell, O. W. Dietrich, and J. Als-Nielsen, Phys. Rev. B **14**, 4897; *ibid.* 4908; *ibid.* 4923 (1976).
- [79] P. M. Horn, J. M. Hastings, and L. M. Corliss, Phys. Rev. Lett. **40**, 126 (1978).
- [80] R. Coldea, R. A. Cowley, T. G. Perring, D. F. McMorrow, and B. Roessli, Phys. Rev. B **57**, 5281 (1998).
- [81] P. Böni, J.L. Martínez, and J.M. Tranquada, Phys. Rev. B **43**, 575 (1991); P. Böni, J.L. Martínez, and J.M. Tranquada, J. Appl. Phys. **67**, 5436 (1990).
- [82] P. Böni, M. Hennion, and J.L. Martínez, Phys. Rev. B **52**, 10142 (1995); P. Böni, B. Roessli, D. Görlitz, J. Kötzler, and J.L. Martínez, Proceedings of the IAEA Technical Committee Meeting on Neutron Beam Research, Lisbon, 68 (1997).
- [83] M.E. Fisher, and A. Aharony, Phys. Rev. Lett. **30**, 559 (1973); *ibid.* Phys. Rev. B **8**, 3342 (1973).
- [84] S.W. Lovesey, J. Phys. Condens. Matter **5**, L251 (1993).
- [85] H. Schinz, and F. Schwabl, Phys. Rev B **57**, 8430 (1998); *ibid.* Phys. Rev B **57** 8438 (1998); *ibid.* **57** 8456 (1998).
- [86] For a review see E. Fawcett, Rev. Mod. Phys. **60**, 209 (1988).
- [87] J. Als-Nielsen, J. D. Axe, and G. Shirane, J. of Appl. Phys. **42**, 1666 (1971).
- [88] R. S. Fishman and S. H. Liu, Phys. Rev. Lett. **76**, 2398 (1996); R. S. Fishman and S. H. Liu, Phys. Rev. B **54**, 7252 (1996).
- [89] J. E. Lorenzo, B. J. Sternlieb, G. Shirane, and S. A. Werner, Phys. Rev. Lett **72**, 1762 (1994).
- [90] P. Böni, B. J. Sternlieb, G. Shirane, B. Roessli, J. E. Lorenzo, and S. A. Werner, Phys. Rev. B **57**, 1057 (1998).
- [91] C. Geibel, C. Schank, S. Thies, H. Kitazawa, C.D. Bredl, A. Bohm, M. Rau, A. Grauel, R. Caspary, R. Helfrich, U. Ahlheim, G. Weber, and F. Steglich, Z. Phys. **B84**, 1 (1991).
- [92] A. Krimmel, P. Fischer, B. Roessli, H. Maletta, C. Geibel, C. Shank, A. Grauel, A. Loidl, and F. Steglich, Z. Phys. **B86**, 161 (1992).
- [93] B.D. Gaulin, D. Gibbs, E.D. Isaacs, J.G. Lussier, J.N. Reimers, A. Schroder, L. Taillefer, P. Zschack, Phys. Rev. Lett. **73**, 890 (1994).
- [94] A. Krimmel, A. Loidl, P. Fischer, B. Roessli, A. Dönni, H. Kita, N. Sato, Y. Endoh, T. Komatsubara, C. Geibel, and F. Steglich, Solid State Comm. **87**, 829 (1993).
- [95] H. Kita, A. Dönni, Y. Endoh, K. Kakurai, N. Sato, and T. Komatsubara, J. Phys. Soc. Japan **63**, 726 (1994).
- [96] T. Petersen, T.E. Mason, G. Aeppli, A.P. Ramirez, E. Bucher, and R.N. Kleimann, Physica **B199**, 151.

- [97] N. Sato, N. Aso, G.H. Lander, B. Roessli, T. Komatsubara, and Y. Endoh, J. Phys. Soc. Japan **66**, 1884 (1997).
- [98] N. Metoki, Y. Haga, Y. Koike, Y. Onuki, Phys. Rev. Lett. **80**, 5417 (1998).
- [99] N. Bernhoeft, A. Hiess, B. Roessli, N. Sato, N. Aso, Y. Endoh, G.H. Lander, and T. Komatsubara, in *Itinerant Electron Magnetism: Fluctuations Effects*, Ed. D. Wagner, W. Brauneck and A. Solontsov, Kluwer, Dordrecht, 43 (1998).
- [100] N. Bernhoeft, N. Sato, B. Roessli, N. Aso, A. Hiess, G.H. Lander, Y. Endoh, and T. Komatsubara, Phys. Rev. Lett. **81**, 4244 (1998).
- [101] N. Bernhoeft, B. Roessli, N. Sato, N. Aso, A. Hiess, G.H. Lander, Y. Endoh, and T. Komatsubara, Physica B **281 & 282**, 993 (2000).
- [102] F.D.M. Haldane, Phys. Lett. **93A**, 464 (1983); Phys. Rev. Lett. **50**, 1153 (1983).
- [103] I. Affleck, J. Phys.: Condens. Matter **1**, 3047 (1989).
- [104] L.P. Regnault, I. Zalizniak, J.P. Renard and C. Vettier, Phys. Rev. B **50**, 9174 (1994) and references therein.
- [105] J. Darriet and L.P. Regnault, Solid State Commun. **86**, 409 (1993).
- [106] M. Enderle, Z. Tun, W.J.L. Buyers, and M. Steiner, Phys. Rev. B **59**, 4235 (1999) and references therein.
- [107] L.P. Regnault and J.P. Renard, Physica B **234-236**, 541 (1997).
- [108] M. Steiner, K. Kakurai, J.K. Kjems, D. Petitgrand, and R. Pynn, J. Appl. Phys. **61**, 3953 (1987).
- [109] S. Raymond, T. Yokoo, A. Zheludev, S.E. Nagler, A. Wildes, and J. Akimitsu, Phys. Rev. Lett. **82**, 2382 (1999).
- [110] I. Affleck, and G.F. Wellman, Phys. Rev. B **46**, 8934 (1992).
- [111] M. Hase, I. Teraski, and K. Uchinokura, Phys. Rev. Lett. **70**, 3651 (1993); J.P. Pouget, L.P. Regnault, M. Aïn, B. Hennion, J.P. Renard, P. Veillet, G. Dhalenne, and A. Revcolevschi, Phys. Rev. Lett. **72**, 4037 (1994).
- [112] M. Nishi, O. Fujita, and J. Akimitsu, Phys. Rev. B **50**, 1105 (1996).
- [113] J.E. Lorenzo, L.P. Regnault, B. Hennion, M. Aïn, F. Bourdarot, J. Kulda, G. Dhalenne and A. Revcolevschi, J. Physics: Cond. Matter **9**, L211-17 (1997); M. Aïn, L.P. Regnault, G. Dhalenne, A. Revcolevschi, and Th. Jolicoeur, J. Appl. Phys. **81**, 4393 (1997).
- [114] M. Steiner, K. Kakurai, and J.K. Kjems, Z. Phys. B **53**, 117 (1983); H.J. Mikeska and M. Steiner, Adv. Phys. **40**, 191 (1991); M. Steiner, in *Magnetic Neutron Scattering*, Ed. A. Furrer, World Scientific, 132 (1995).
- [115] J.P. Boucher, L.P. Regnault, R. Pynn, J. Bouillot, J.P. Renard, Europhys. Lett. **1**, 415 (1986).
- [116] S.K. Sinha and D.K. Ross, Physica B **149**, 51 (1988).

- [117] S.V. Maleyev, Phys. Rev. Lett. **75**, 4682 (1995).
- [118] L.P. Regnault, F. Tasset, J.E. Lorenzo, T. Roberts, G. Dhalenne, and A. Revcolevschi, Physica B **267-268**, 227 (1999).
- [119] P.J. Brown, I.K. Jassim, K.-U. Neumann, and K.R.A. Ziebeck, Physica B **161**, 9 (1989).

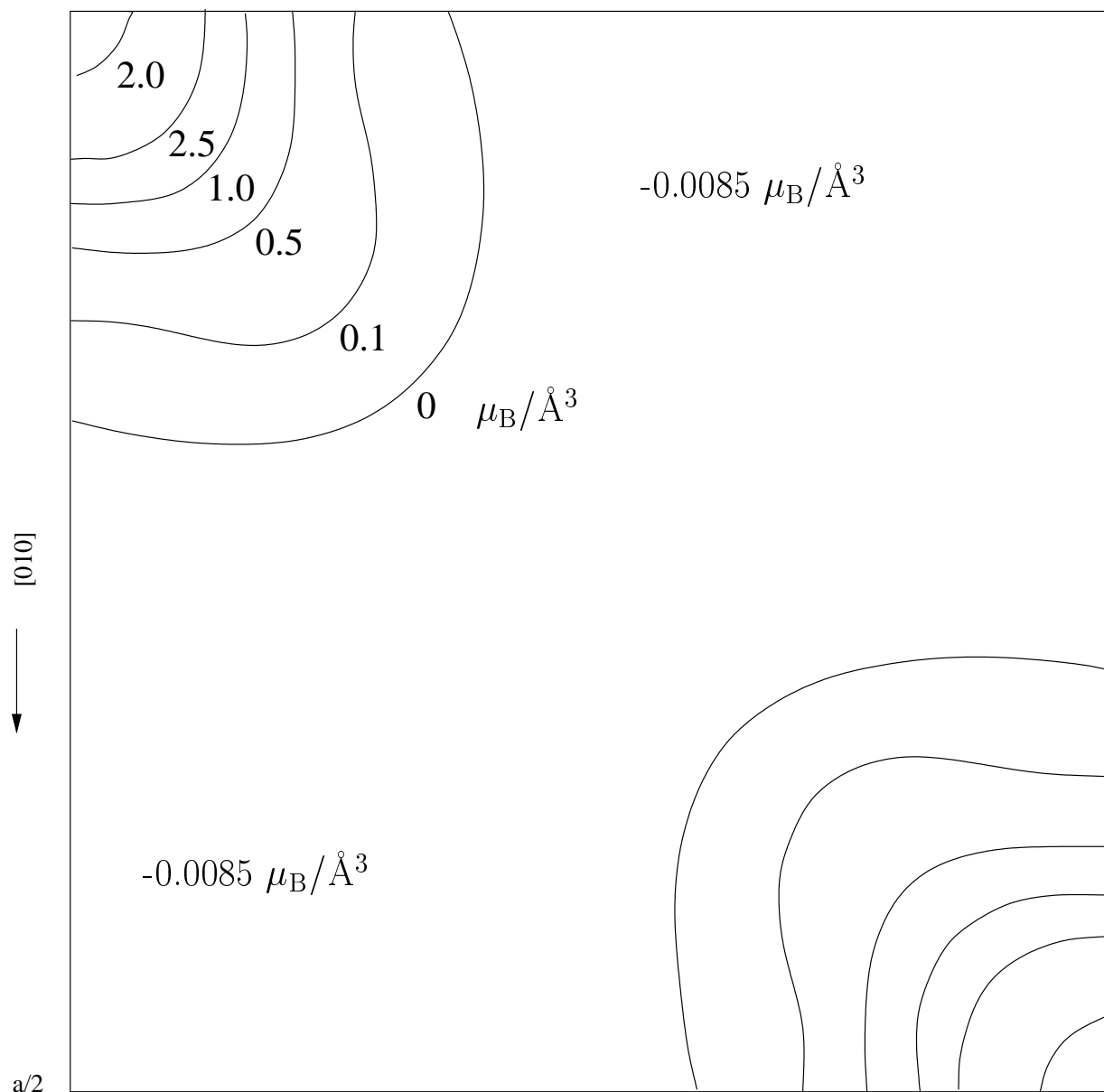




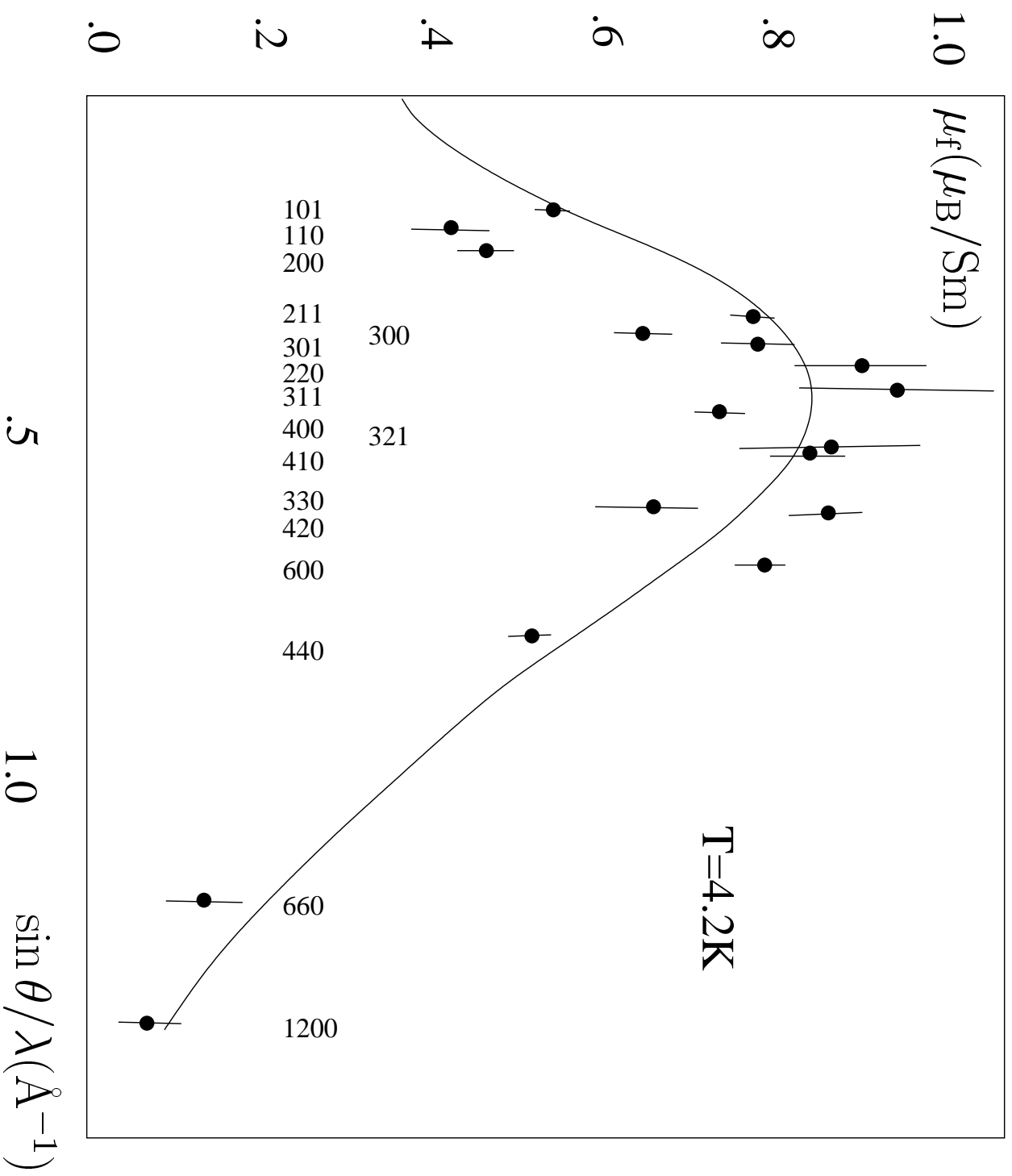
NICKEL  
NUCLEUS

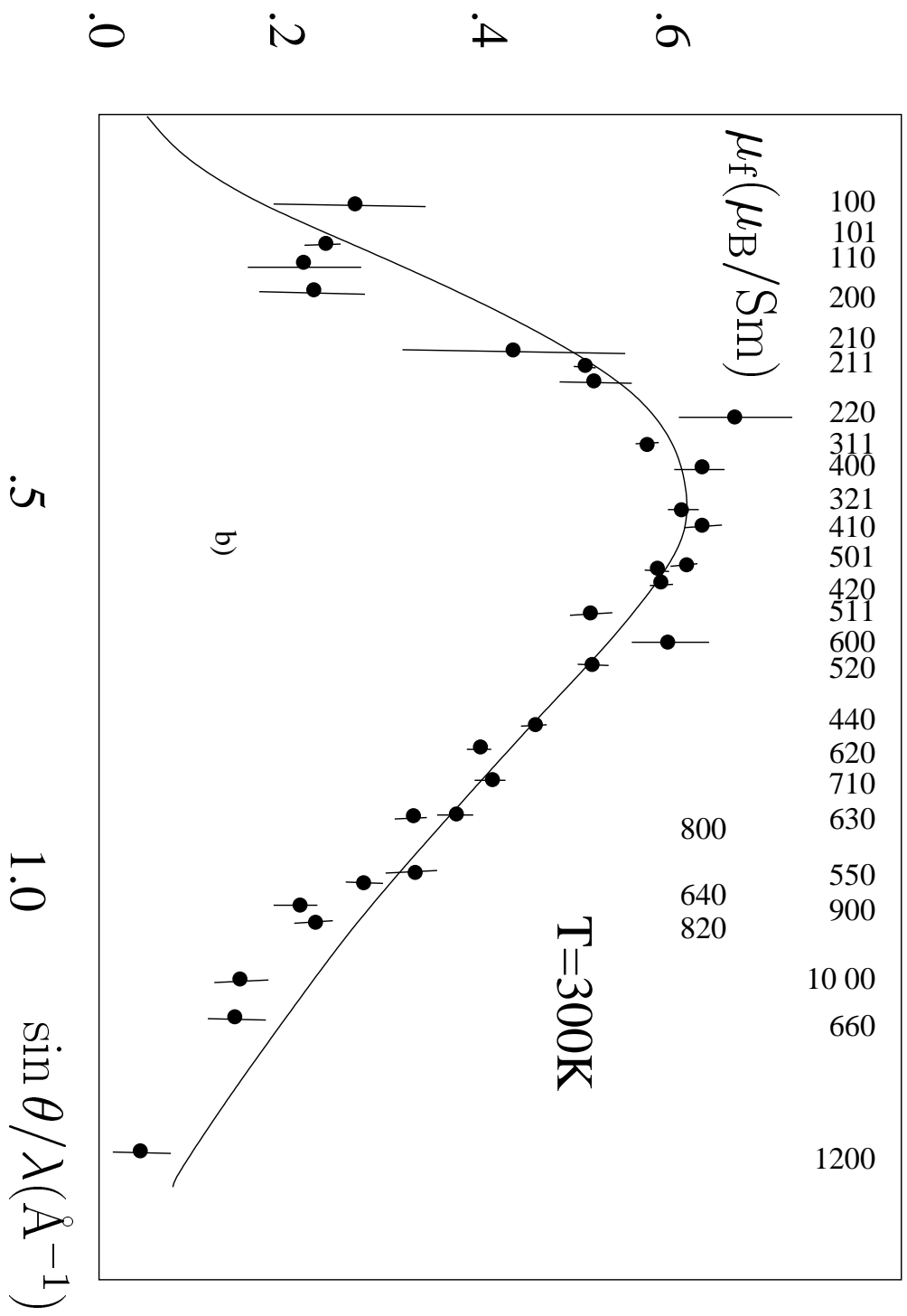
[100]  $\longrightarrow$

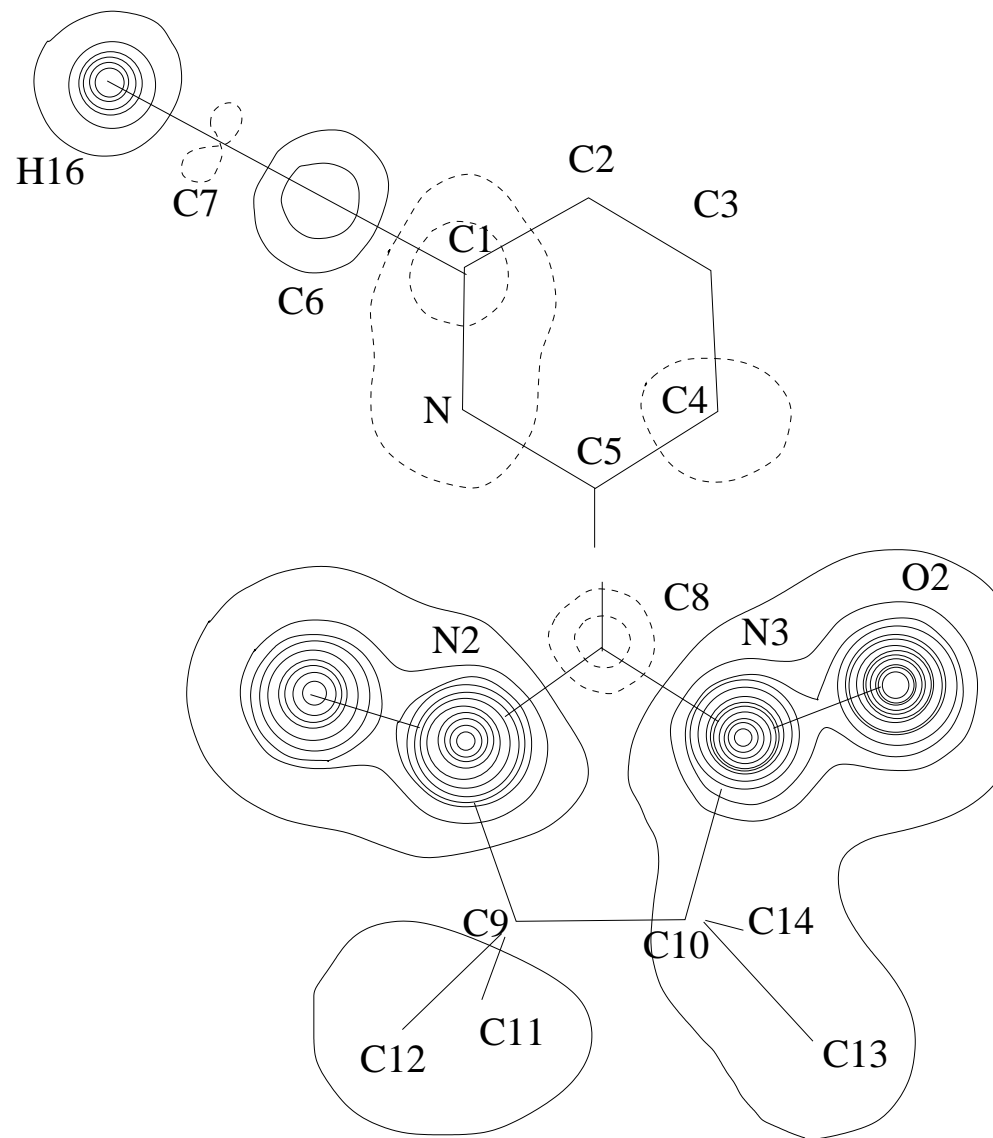
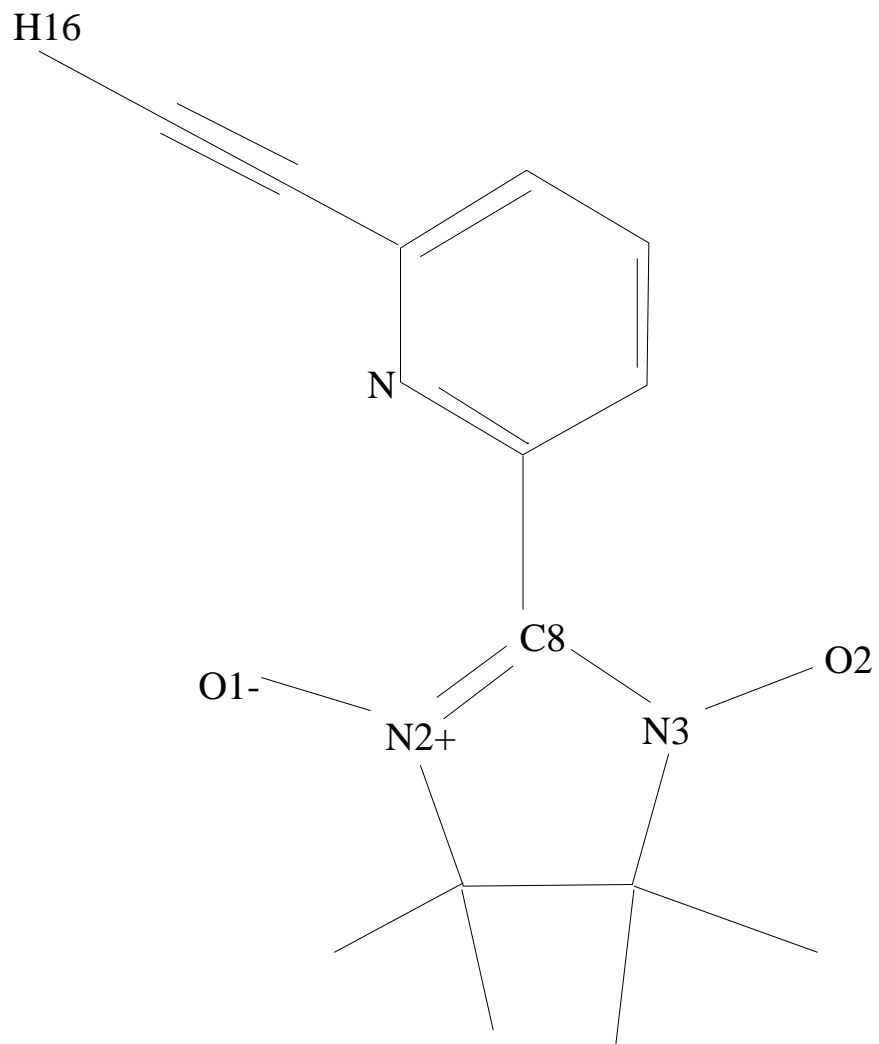
a/2



NICKEL  
NUCLEUS







Mn

O1

C2

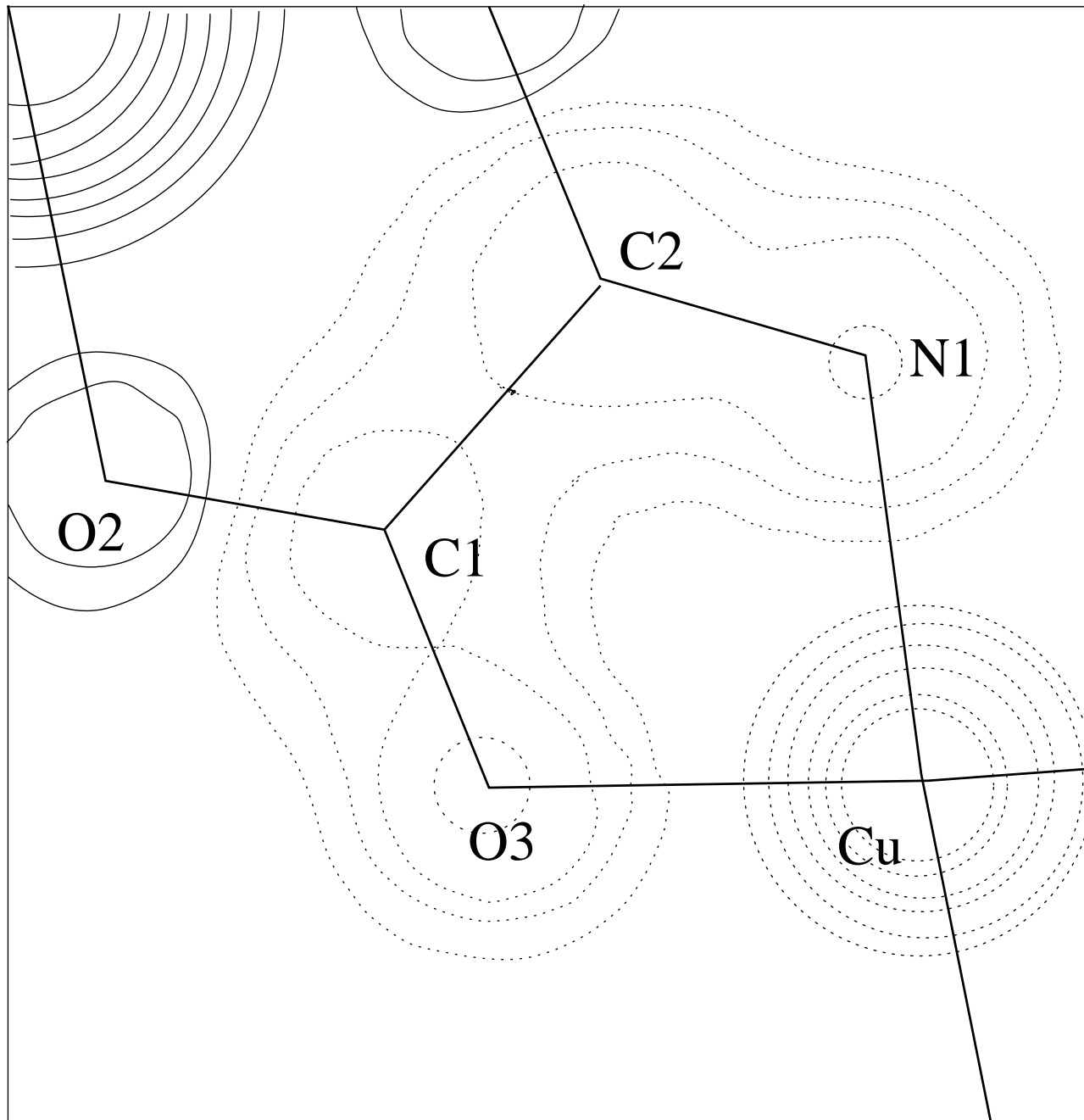
N1

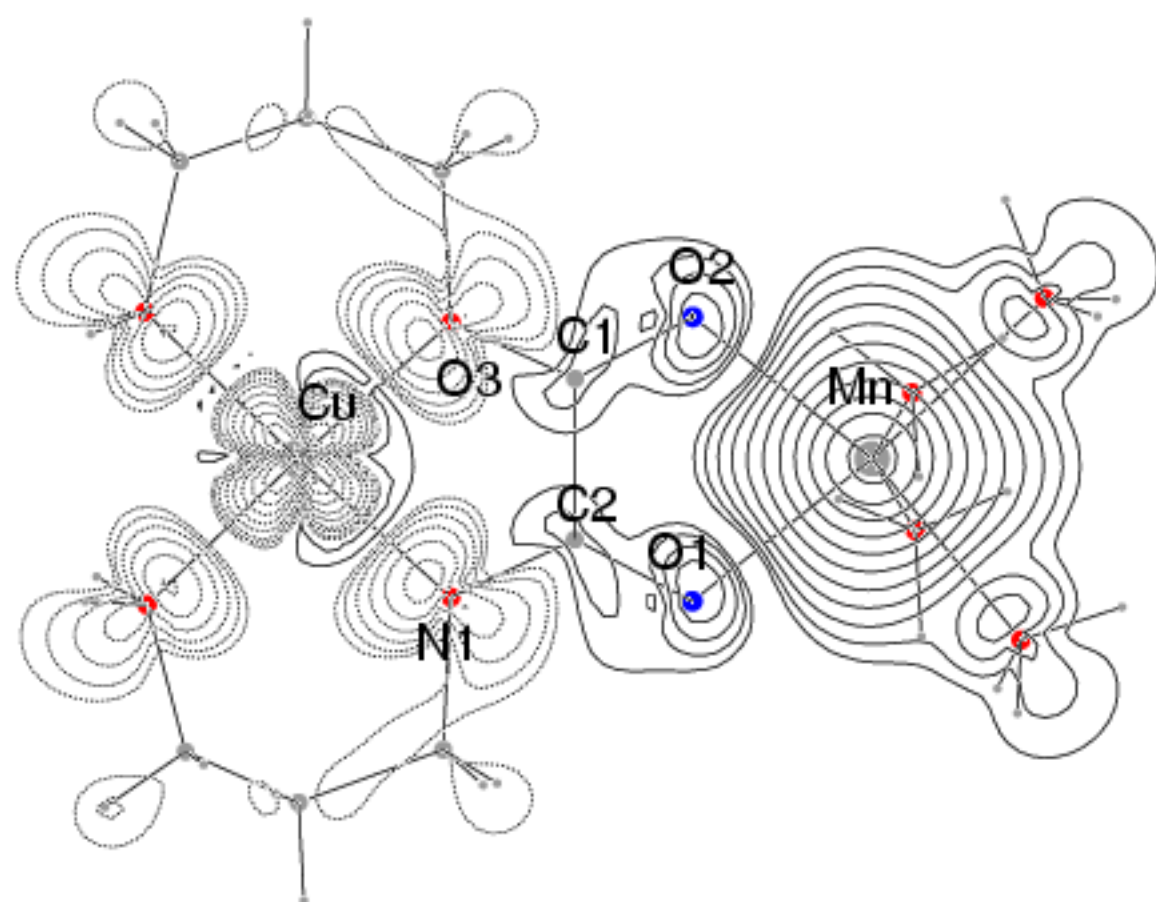
O2

C1

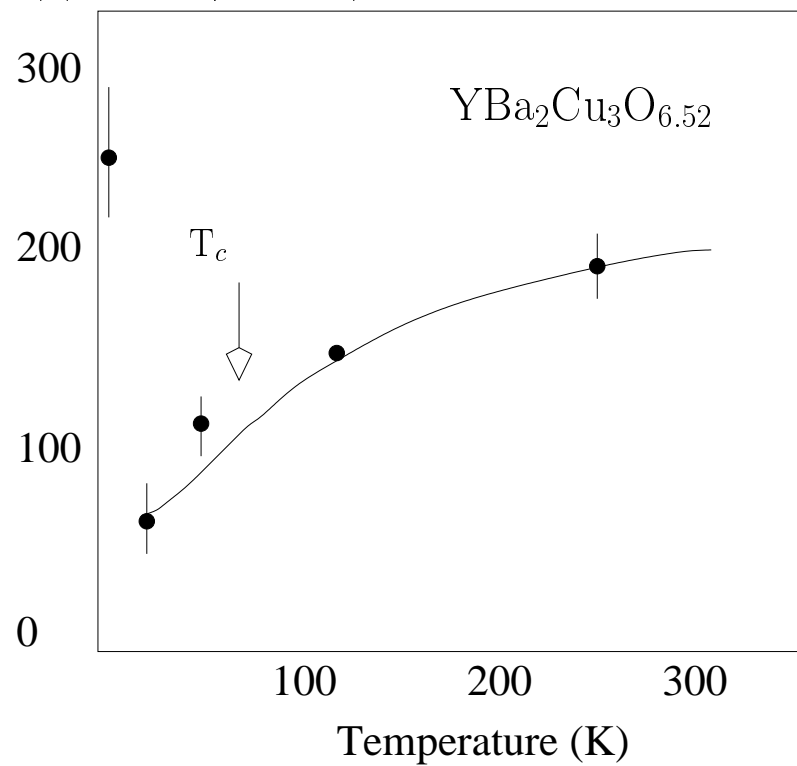
O3

Cu

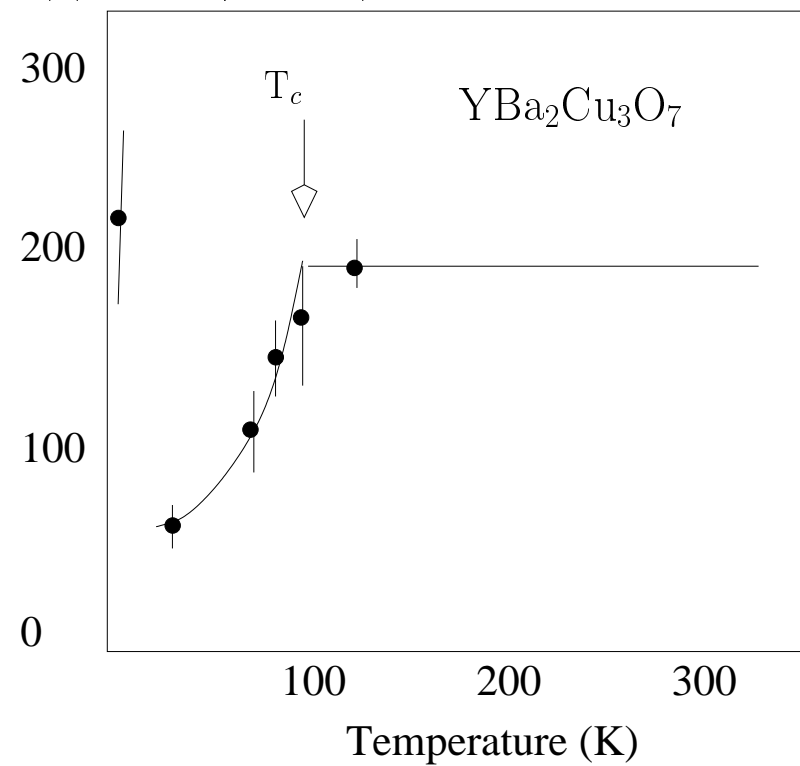




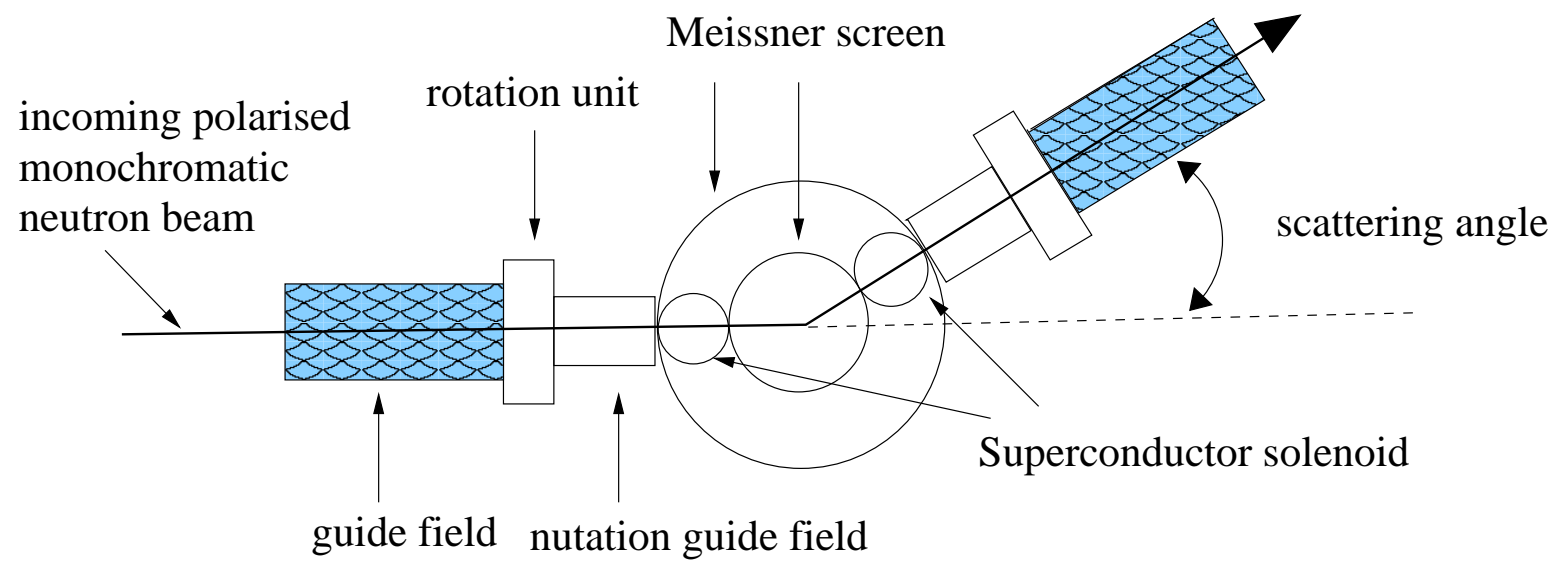
$\chi(Cu)(10^{-6}\mu_B/Tesla)$

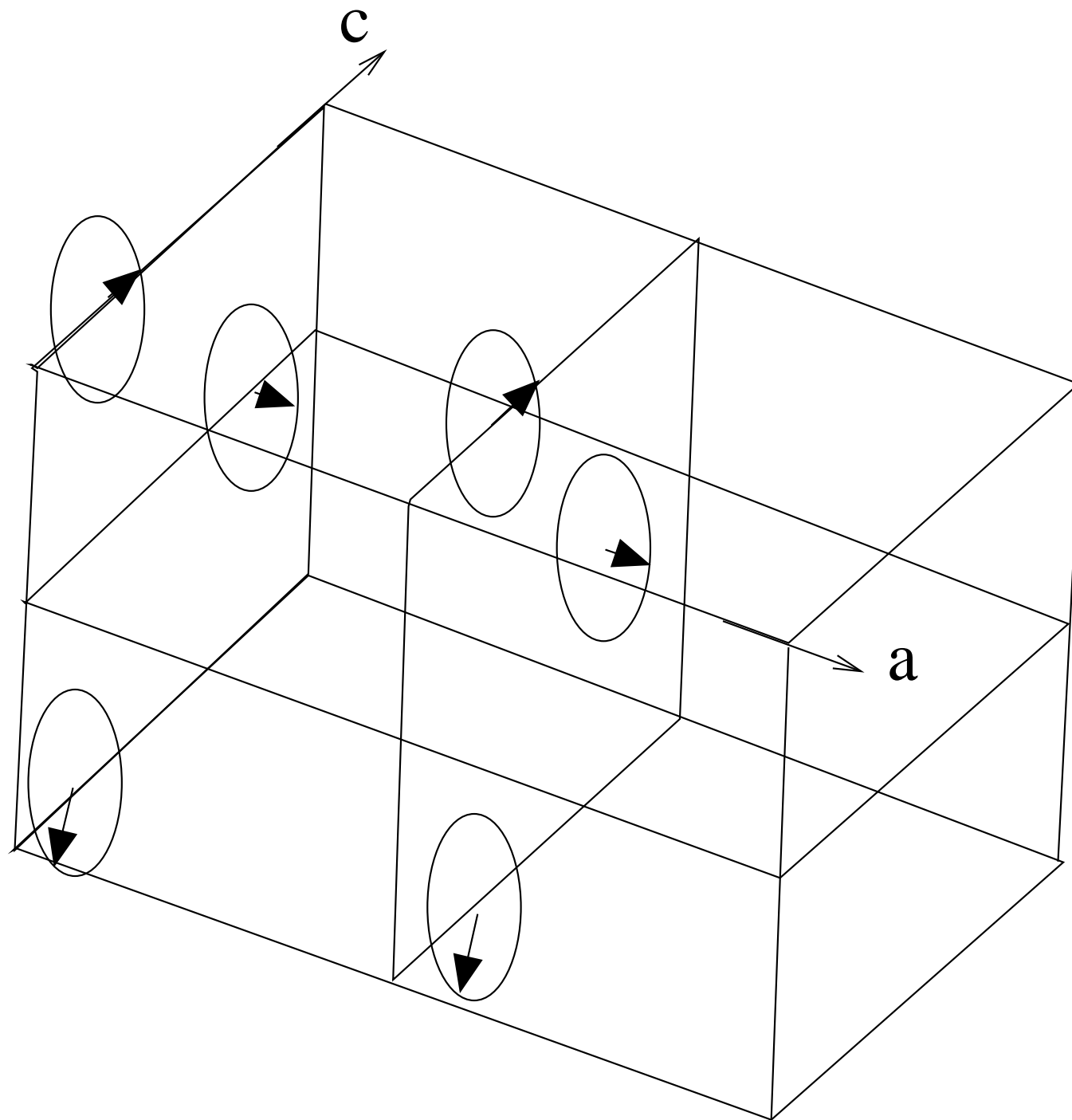


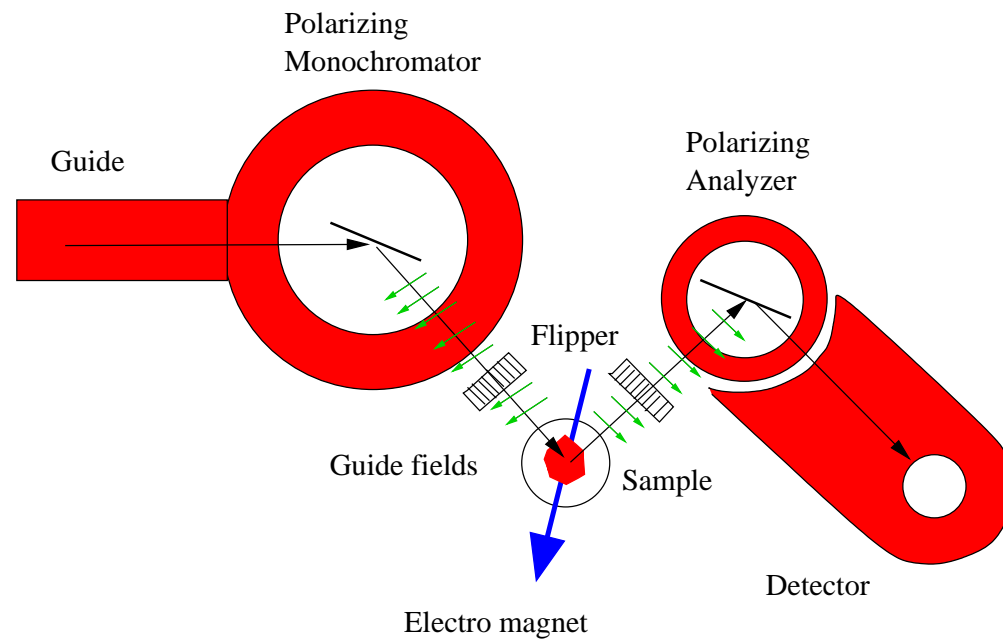
$\chi(Cu)(10^{-6}\mu_B/Tesla)$

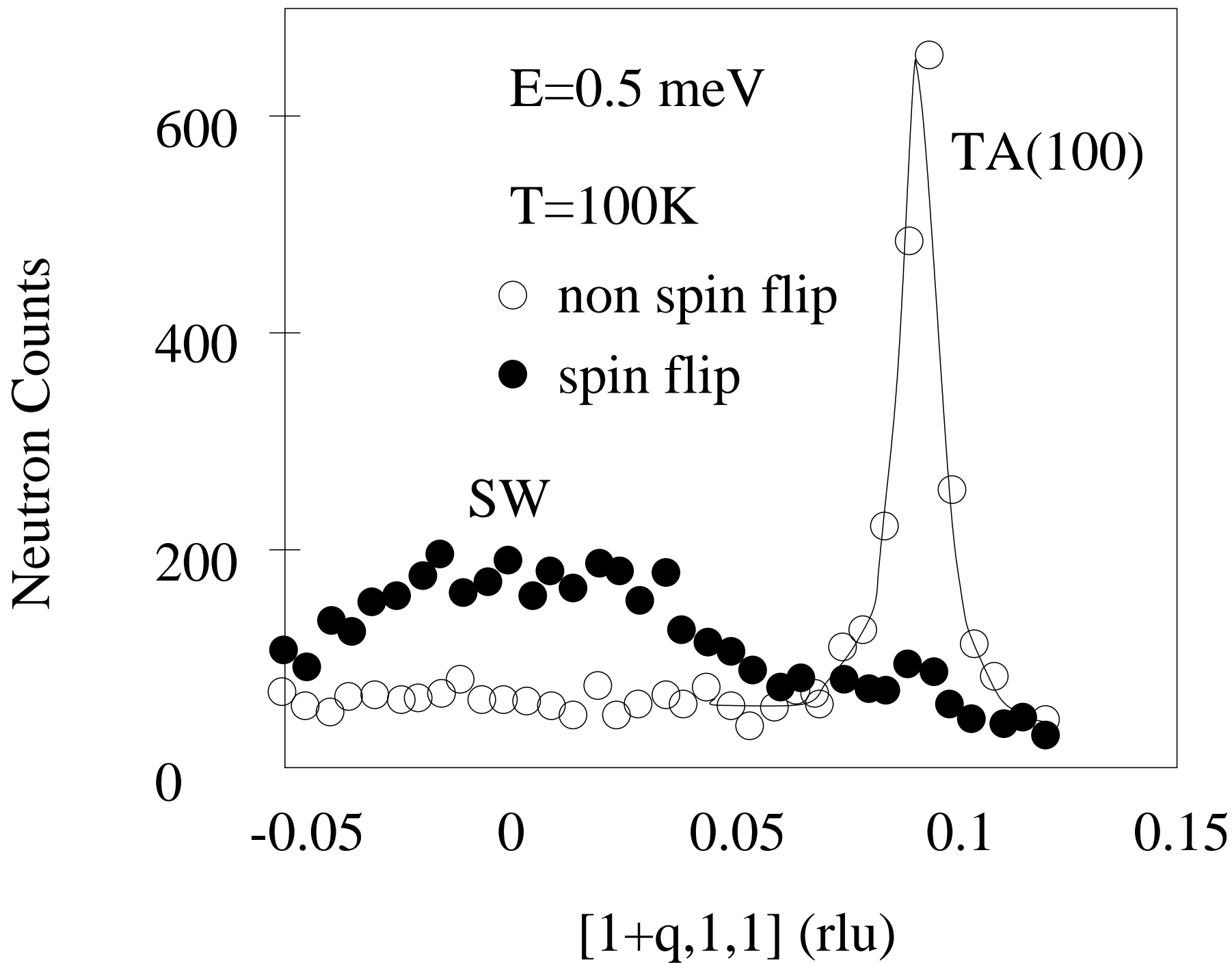


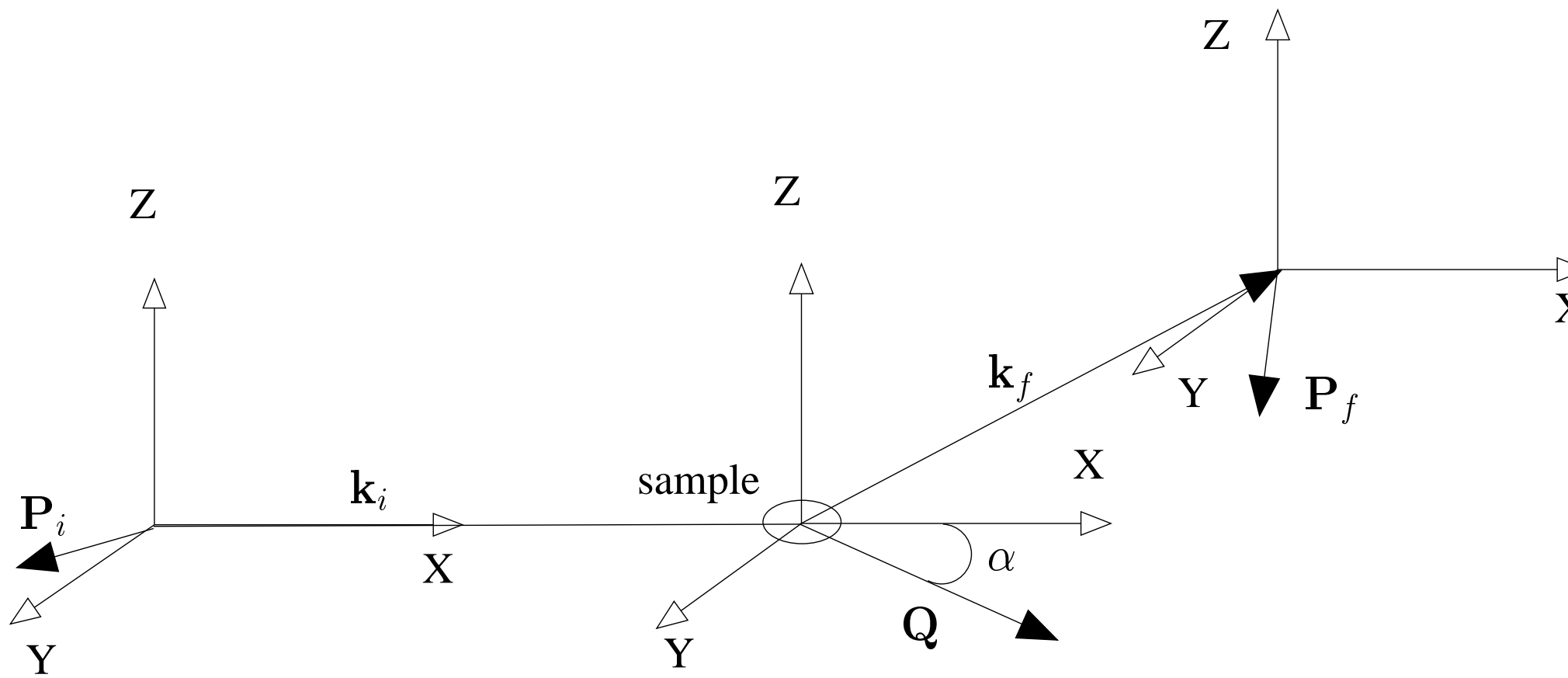




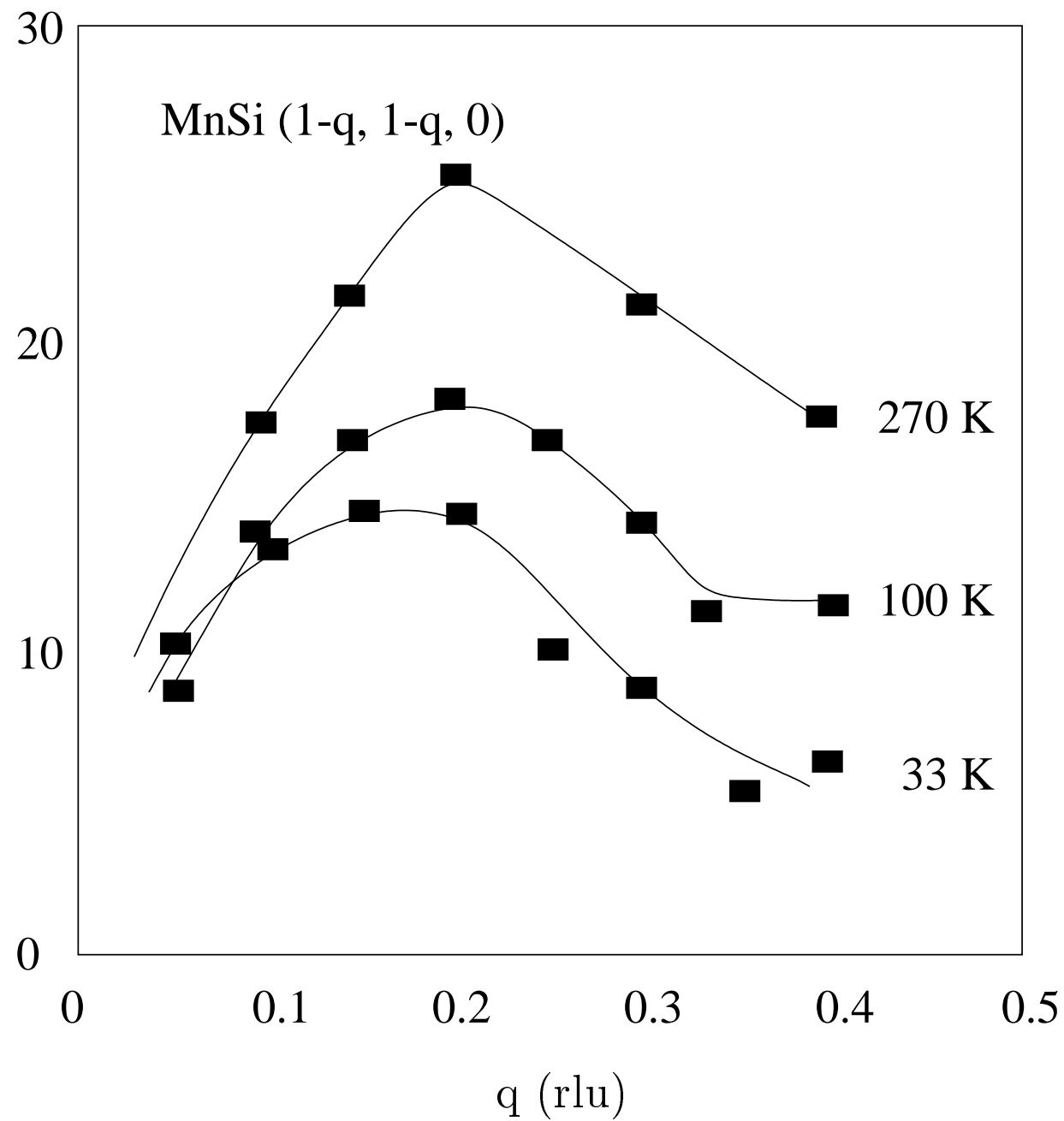








$$4\pi q^2 < M_q^2 > (\mu_B^2)$$



$E_i = 2.98 \text{ meV}$  42-41-EuS-37-40  $T = 0.93 T_c$

